

1      **The eddy-driven jet and storm-track responses to boundary-layer drag:**  
2      **insights from an idealized dry GCM study**

3      Cheikh O. Mbengue\* and Tim Woollings

4      *University of Oxford, Oxford, United Kingdom*

5      \*Corresponding author address: Cheikh Oumar Mbengue, Atmospheric, Oceanic, and Planetary  
6      Physics, Sherrington Road, Oxford OX1 3PU, United Kingdom.  
7      E-mail: c.mbengue@wolfson.oxon.org

## ABSTRACT

8     Simulations using a dry, idealized general circulation model (GCM) are con-  
9     ducted to systematically investigate the eddy-driven jet's sensitivity to the lo-  
10    cation of boundary-layer drag. Perturbations of boundary-layer drag solely  
11    within the baroclinic zone reproduce the eddy-driven jet responses to global  
12    drag variations. The implications for current theories of eddy-driven jet shifts  
13    are discussed. Hemispherically-asymmetric drag simulations in equinoctial  
14    and solstitial thermal conditions show that perturbations of surface drag in  
15    one hemisphere have negligible effects on the strength and latitude of the  
16    eddy-driven jet in the opposite hemisphere. Jet speed exhibits larger sensitiv-  
17    ties to surface drag in perpetual winter simulations, while sensitivities in jet  
18    latitude are larger in perpetual summer simulations. Near-surface drag simu-  
19    lations with an Earth-like continental profile show how surface drag may facil-  
20    itate tropical-extratropical teleconnections by modifying waveguides through  
21    changes in jet latitude. Longitudinally confined drag simulations demonstrate  
22    a novel mechanism for localizing storm tracks. A theoretical analysis is used  
23    to show that asymmetries in the Bernoulli function within the baroclinic zone  
24    are important for the eddy-driven jet latitude responses because they directly  
25    modulate the sensitivity of the zonal-mean zonal wind to drag in the boundary-  
26    layer momentum balance. The simulations contained herein provide a rich  
27    array of case studies against which to test current theories of eddy-driven jet  
28    and storm-track shifts; and the results affirm the importance of correct, well-  
29    constrained locations and intensities of boundary-layer drag in order to reduce  
30    jet and storm-track biases in climate and forecast models.

31 **1. Introduction**

32 Momentum mixing and dissipation play important roles in the Earth’s atmospheric energy cycle  
33 and momentum budget (Lorenz 1955; Phillips 1956). Early climate models used drag parameters  
34 to address biases in the models’ climate (Stephenson 1994)—while drag parameters today are  
35 semi-empirical and not well constrained. As a result, a body of research has developed around  
36 the impacts of subgrid-scale drag parameterizations on major features of the general circulation  
37 (James and Gray 1986; Stephenson 1994, 1995; Robinson 1997; Chen et al. 2007; Kidston and  
38 Vallis 2010; Sandu et al. 2016; Polichtchouk and Shepherd 2016; Pithan et al. 2016). One such  
39 feature is the eddy-driven jet.

40 Theoretical studies of the eddy-driven jet response to drag focused primarily on global drag  
41 variations (James and Gray 1986; Robinson 1997; Chen et al. 2007; Kidston and Vallis 2010;  
42 Polichtchouk and Shepherd 2016), although counterexamples exist; e.g., variations in parameter-  
43 ized gravity wave (Stephenson 1994) and blocking drag are necessarily local because they depend  
44 on the variance of subgrid-scale orography<sup>1</sup>. These studies have shown that the eddy-driven jet  
45 shifts equatorward when gravity-wave and near-surface drag are increased (James and Gray 1986;  
46 Stephenson 1994; Robinson 1997; Chen et al. 2007); while increases in hyperdiffusivity shift the  
47 jet poleward (Stephenson 1995), although questions remain about the dependence of this result on  
48 model resolution. A recent study has linked model biases to the quality and intensity of block-  
49 ing drag parameterization (Pithan et al. 2016), and has called for improvements in low-level drag  
50 parameterizations in coarse-resolution climate models.

51 Their study highlights the need for regional idealized drag simulations to elucidate and refine  
52 current theories of eddy-driven jet shifts; this motivates the current study.

---

<sup>1</sup>We do not consider the dynamics of resolved-scale orography.

53 Several momentum sinks may exist in an atmosphere; however, here, we conduct simulations  
54 using a dry dynamical core and focus only on near-surface, boundary-layer drag. We use dry,  
55 idealized simulations as a starting point for several reasons: 1) to determine the extent to which  
56 dry processes account for the eddy-driven jet's response to surface drag, 2) to isolate the impact  
57 of surface drag from changes in drag due to moist processes. For example, the latent heat release  
58 associated with moist convection in the tropics may increase the strength of the tropical overturning  
59 circulation, which increases the surface winds. Surface drag then acts to reduce those winds,  
60 which in turn modifies surface sensible and latent heat fluxes. 3) To remove the effect of drag  
61 on moist processes, like surface evaporation. 4) To reduce the incidence of simultaneous actors,  
62 which increases the chances of identifying causal relationships. We use quadratic drag and build  
63 upon previous work that used linear drag to understand the eddy-driven jet response to boundary-  
64 layer drag in an idealized framework. Furthermore, we conduct numerous simulations over a wide  
65 quadratic-drag parameter space.

66 There exist several proposed mechanisms for jet shifts in response to external forcing. One  
67 school of thought posits that changes in the spectral character of the extratropical eddies that con-  
68 verge momentum into the jet are primarily responsible for changes in jet latitude. For example,  
69 Chen et al. (2007) suggest that an increase in the eastward phase-speed of baroclinic eddies that  
70 accompanies an increase in the speed of the eddy-driven jet shifts the jet poleward. But a com-  
71 prehensive survey of the eddy-driven jets sensitivity to localized Gaussian heating in the latitude-  
72 sigma plane (Baker et al. 2017) shows a range of forcing for which the jet shifts poleward even  
73 though the eddy-driven jet's speed decreases. Thus, an increase in the eastward phase speed of  
74 eddies does not always accompany poleward jet shifts—although, it frequently does in idealized  
75 studies in response to common forcings (e.g. Robinson 1997; Chen et al. 2007; Barnes et al. 2010;  
76 Kidston and Vallis 2012; Lorenz 2014). To reconcile this apparent contradiction and building on

<sup>77</sup> the work of Kidston and Vallis (2012), Lorenz (2014) argued that a decrease in the eddy-driven  
<sup>78</sup> jet speed could shift the eddy-driven jet poleward because lower phase-speed eddies are preferen-  
<sup>79</sup> tially reflected poleward of the jet—instead of meeting and breaking at their critical latitude. This  
<sup>80</sup> enhanced reflection implies reduced deceleration on the poleward side of the jet and a poleward  
<sup>81</sup> shift or extension of the eddy-driven jet.

<sup>82</sup> But another school of thought argues that changes in baroclinic driving initiate and maintain  
<sup>83</sup> changes in the eddy driven jet’s speed and latitude. In midlatitudes, baroclinic eddies, the product  
<sup>84</sup> of baroclinic instability (Charney 1947; Eady 1949), converge angular momentum into the jet and,  
<sup>85</sup> in a statistically steady state, balance westerly momentum loss at the surface. Therefore, it is  
<sup>86</sup> reasonable to expect this driving to exert dominant, first-order control on the characteristics of the  
<sup>87</sup> eddy-driven jet. Several studies report changes in jet speed or latitude in response to changes in  
<sup>88</sup> baroclinicity (e.g. Yin 2005; Brayshaw et al. 2008; Mbengue and Schneider 2017; Baker et al.  
<sup>89</sup> 2017). In fact, some studies suggest that the changes in the spectral character of the eddies that  
<sup>90</sup> accelerate the jet are, in fact, part of the effect of more fundamental causes, like changes in the jet  
<sup>91</sup> or the baroclinicity itself (Barnes and Hartmann 2011; Baker et al. 2017; Mbengue and Schneider  
<sup>92</sup> 2018). Yet still other studies suggest that the dynamics of barotropic instabilities and shears play  
<sup>93</sup> an important role in jet responses (James and Gray 1986; James 1987).

<sup>94</sup> Idealized simulations have proven useful in helping to disentangle simultaneous actors and to  
<sup>95</sup> help establish and understand causal relationships. Here, we extend the work of previous authors  
<sup>96</sup> on the storm-track and jet response to near-surface drag beyond global-drag simulations to gain  
<sup>97</sup> further insight. We suggest how the responses might relate to those in more complex models.  
<sup>98</sup> Finally, we present a simple theory that explains the eddy-driven jet latitude response seen in our  
<sup>99</sup> simulations. Section 2 follows with a description of the GCM and the simulations conducted in

100 this study. Section 3 presents the results and section 4 discusses them. Finally, concluding remarks  
101 are made in section 5.

102 **2. Model and Simulations**

103 GFDL’s Flexible Modeling system (FMS) is used to investigate the eddy-driven jet’s response  
104 to perturbations in near-surface drag. The GCM is a three-dimensional, turbulent model, with a  
105 dry dynamical core and a set of dry physics schemes. The GCM solves the primitive equations on  
106 a sphere using a spectral transform method and is run at T42 spectral resolution. T85- and T127-  
107 resolution simulations were used to check the robustness of the results. The results are robust.  
108 The model has 30 unevenly distributed  $\sigma$  levels ( $\sigma = p/p_s$ , where  $p$  is pressure and  $p_s$  is surface  
109 pressure).

110 Radiative fluxes are parametrized using Newtonian relaxation toward a prescribed, semi-gray  
111 radiative-equilibrium profile. The equilibrium profile is statically unstable in the lower tropo-  
112 sphere (Schneider 2004). The profile is the same one used in Schneider and Walker (2006)  
113 and Mbengue and Schneider (2013) in all but the solstitial-profile simulations, in which a new  
114 radiative-equilibrium surface temperature, which shifts the subsolar point off of the equator, is  
115 defined as,

$$T_s^e(\varphi) = \overline{T}_s^e + \Delta_h \left( \frac{1}{3} + 2 \sin(\varphi_0) \sin \varphi - \sin^2 \varphi \right), \quad (1)$$

116 where  $\varphi$  is latitude,  $\varphi_0$  is the latitude of the sub-solar point,  $T_s^e$  is the equilibrium surface tempera-  
117 ture, and  $\Delta_h$  is the pole-to-equator thermal contrast. The overline  $(\cdot)$  in (1) signifies a global mean.  
118 A quasi-equilibrium dry convection scheme, also described in Mbengue and Schneider (2013),  
119 relaxes temperatures within an atmospheric column toward a prescribed 6.9 K/km lapse rate in  
120 an energetically consistent way. The radiative forcing is constant throughout a given simulation:  
121 there are no diurnal or seasonal cycles. The surface is thermally insulated and has no topography.

122 Surface momentum transfer is modeled using quadratic skin friction. The drag coefficient is  
123 computed using Monin-Obukhov similarity theory. The default surface roughness is  $5 \times 10^{-3}$   
124 m; and the scheme uses a 1 m/s constant gustiness. A vertical diffusion parametrization diffuses  
125 dry static energy within a fixed-height, 2500 m planetary boundary layer. Horizontal  $\nabla^8$  hyper-  
126 diffusion acts at the smallest resolved scales. All simulations are run for at least 1800 days. More  
127 complex configurations require longer integrations to attain a statistically steady state.

128 *a. The eddy-driven jet*

129 In contrast to the subtropical jet, the eddy-driven jet is structurally barotropic. The mechanics of  
130 the eddy-driven jet differ from those of the subtropical jet: in the zonal mean, the eddy-driven jet  
131 owes its existence to baroclinic eddies, which converge angular momentum into midlatitudes to  
132 balance momentum loss at the surface. This convergence occurs primarily in the upper troposphere  
133 (Ait-Chaalal and Schneider 2015), but downward momentum transport through wave dynamics  
134 and residual, eddy-driven circulations barotropizes the jet, thus determining the surface winds.  
135 An equivalent barotropic structure of the extratropical jet emerges when meridional temperature  
136 gradients impose a vertical wind shear on the flow. Therefore, given the nature of the eddy-driven  
137 jet and following previous authors, near-surface winds are used as a proxy for the eddy-driven jet  
138 (Woollings et al. 2010). In this study, the term near-surface refers to a vertical average between  
139  $\sigma = 0.8$  and  $\sigma = 0.6$ .

140 *b. Boundary-layer drag parametrization*

141 In addition to the skin-friction drag parametrization in the GCM, whose parameters are unper-  
142 turbed, we add a quadratic drag parametrization which retards the near-surface winds—a quadratic  
143 drag parametrization is an improvement over a linear, Rayleigh drag parametrization, which is

<sup>144</sup> common in idealized studies. The enhanced drag is given by,

$$\frac{D\mathbf{V}}{Dt} = \dots - c_D S(\varphi, \lambda, p) |\mathbf{V}| \mathbf{V}, \quad (2)$$

<sup>145</sup> where  $\mathbf{V}$  is the horizontal velocity vector,  $|\mathbf{V}| = \sqrt{u^2 + v^2}$ , where  $u$  and  $v$  are the eastward and  
<sup>146</sup> northward components of the wind,  $c_D$  is the quadratic drag coefficient, the parameter in this  
<sup>147</sup> study,  $S(\varphi, \lambda, p)$  is a three-dimensional shape function that defines the spatial distribution of the  
<sup>148</sup> boundary-layer drag. The horizontal spatial coordinates  $\varphi$  and  $\lambda$  represent latitude and longitude.  
<sup>149</sup> The boundary-layer drag attains a maximum at the lowest grid level and decreases linearly to zero  
<sup>150</sup> at the top of the boundary layer. In regions where the boundary-layer drag is enhanced, it assumes  
<sup>151</sup> a constant value in the horizontal plane. Note that ‘no drag’ in this paper refers to no *enhanced*  
<sup>152</sup> drag: all simulations have surface dissipation.

<sup>153</sup> The radiation and convection parametrizations improve the tropical thermal stratification and the  
<sup>154</sup> tropical tropopause height of the standard Held and Suarez (1994) configuration, which is really  
<sup>155</sup> a benchmark for dry dynamical cores. Furthermore, the model does not have significant near-  
<sup>156</sup> surface eddy temperature variances penetrating into deep tropics. Hence, tropical and extratropical  
<sup>157</sup> dynamics interact in a more realistic way. Because we use contemporary drag parametrizations  
<sup>158</sup> in concert with the aforementioned radiation and convection parametrizations, our simulations are  
<sup>159</sup> the most realistic idealized, dry simulations to date to investigate the eddy-driven jet’s response to  
<sup>160</sup> near-surface drag.

<sup>161</sup> *c. Covariance spectral analysis*

<sup>162</sup> To compute the northward temperature and momentum flux co-spectra, the method of Hayashi  
<sup>163</sup> (1971) is used. This method differentiates between forward and rearward propagating waves, and  
<sup>164</sup> has found extensive use in the atmospheric science community (e.g. Randel and Held 1991; Chen

et al. 2007). A 30-member 90-day ensemble is used to compute the co-spectra. The resultant four-dimensional output is a function of ensemble size, latitude, time, and longitude. Fourier transforms in time and longitude transform the model output into ensemble, latitude, frequency, and wave number. The frequency and wave number are converted to frequency and phase speed,  $c = \omega a \cos \varphi / n$  (Randel and Held 1991), where  $\omega$  is the frequency,  $a$  is the planetary radius,  $n$  is the wave number, and  $\varphi$  is latitude. Summing over all wave numbers and then taking the ensemble mean yields model output that is a function of latitude and phase speed. The phase speeds are interpolated onto a 1 m/s resolution grid. In the plots of the phase-speed spectra, the control simulation represents an unperturbed simulation, while quadratic drag with a coefficient of  $128 \times 10^{-7} \text{ m}^{-1}$  is added in the perturbed simulations. The large value ensures an easily detectable steady-state response.

#### 176 d. Continent-profile drag simulations

To compare and contrast changes in boundary-layer friction over land versus over ocean, simulations are conducted in which boundary-layer friction is modeled as,

$$c_D = c_{D,O} \times \%H_2O + c_{D,L} \times (1 - \%H_2O), \quad (3)$$

where  $C_{D,O}$  represents the drag coefficient over the ocean,  $C_{D,L}$  represents the drag coefficient over the continents, and  $\%H_2O$  is the fraction of water covering a grid cell. Regions of sea ice are treated as ocean. Four simulations, which we refer to as continent-profile simulations, are conducted. Their drag distributions are detailed in Table 1.

#### 183 e. Zonally-symmetric and hemispherically-symmetric boundary-layer drag simulations

Three groups of zonally-symmetric boundary-layer friction simulations are conducted. In one set of simulations—which follows previous studies—drag is varied globally and the changes in

186 the speed and latitude of the eddy-driven jet are observed. In these global drag simulations, the  
187 drag coefficient  $C_D$  is varied from  $1 \times 10^{-7} \text{ m}^{-1}$  to  $1024 \times 10^{-7} \text{ m}^{-1}$ . To separate the effects of  
188 global variations in drag from localized but zonally symmetric variations in drag, simulations are  
189 conducted in which drag is varied solely within the baroclinic zone. These simulations are referred  
190 to as baroclinic-zone drag simulations. The baroclinic zone is considered to be the constant-width  
191 regions between  $\pm 35^\circ\text{N}$  and  $\pm 55^\circ\text{N}$ . The baroclinic zone width is large enough that the eddy-  
192 driven jet maximum remains within the baroclinic zone over all simulations.

193 A set of zonally-symmetric simulations, referred to as banded friction simulations, is conducted  
194 in which near-surface hemispherically-symmetric drag is turned on progressively in  $10^\circ$  bands  
195 starting at the equator and moving poleward. The jet speed and latitude response are then observed.  
196 In these experiments, the drag coefficient where the friction is turned on is  $200 \times 10^{-7} \text{ m}^{-1}$ . A  
197 large drag coefficient is used in this experiment to ensure that the response is easy to identify.

#### 198 *f. Zonally-symmetric and hemispherically-asymmetric boundary-layer drag simulations*

199 A novel set of simulations in which the drag coefficient is varied solely within one hemisphere  
200 and the jet response observed is also conducted. The Northern-Southern Hemisphere asymmetries  
201 on Earth make these simulations especially relevant. In these simulations, drag is varied from  
202  $5 \times 10^{-7} \text{ m}^{-1}$  to  $1200 \times 10^{-7} \text{ m}^{-1}$ .

203 The last set of simulations shift the subsolar point 10 degrees latitude into one hemisphere to  
204 mimic a winter and summer hemisphere. Then, the drag is modified in one hemisphere and the  
205 eddy-driven jet speed and latitude responses are observed. These simulations elucidate the sea-  
206 sonal jet response to changes in near-surface drag.

207 **3. Results**

208 *a. Global drag simulations*

209 The maximum zonal-mean jet speed decreases as boundary-layer drag increases, see Figure 1a.  
210 Changes in boundary-layer quadratic drag over two orders of magnitude modifies the jet maximum  
211 over a range of about 5 m/s. At high drag values, an increase in boundary-layer drag slightly  
212 increases the jet speed (Figure 1). The shape of the jet maximum curve is sigmoid-like when  
213 plotted on a log-linear axis; that is, the slope of the curve at high and low values are modest  
214 compared to the center parts of the curve. As anticipated from the quadratic nature of the drag  
215 parameterization, the zonal-mean jet speed and latitude responses to boundary-layer friction are  
216 nonlinear.

217 As the boundary-layer drag increases, the jet shifts equatorward (Figure 1b). This result agrees  
218 with previous idealized work, albeit with linear, Rayleigh drag, that shows an equatorward jet shift  
219 with increased drag. The jet-latitude curve is also sigmoidal, but shows greater curvature when  
220 compared to the jet-speed curve. The uncertainty is greater in the jet-latitude response. The jet  
221 position has a 12-degree latitude range over the simulated drag parameter space.

222 *Meridionally-asymmetric, zonally-symmetric drag simulations*

223 Boundary-layer drag increasing solely within the baroclinic zone reduces the near-surface west-  
224 erly wind maximum speed and shifts the eddy-driven jet equatorward (Figure 2a; b). The baro-  
225 clinic zone is the region of highest baroclinic activity. Here we assume it to be the region within  
226  $\pm 35^{\circ}\text{N}$  and  $\pm 55^{\circ}\text{N}$ . The baroclinic zone encloses the eddy-driven jet maximum in all simulations.  
227 The drag coefficient used in these baroclinic zone simulations is  $64 \times 10^{-7} \text{ m}^{-1}$ .

228     Figure 2c shows the zonal-mean eddy-driven jet speed response to boundary-layer drag that  
229     extends from the equator to the latitude specified on the abscissa; Figure 2d shows the eddy-driven  
230     jet-latitude response. The boundary-layer friction is turned on in increments of  $10^{\circ}$  latitude in the  
231     direction of the black arrow in the figure. The blue dots show the jet in the Southern Hemisphere,  
232     while the red dots show the statistically independent jet in the Northern Hemisphere. Figure 2  
233     shows that the eddy-driven jet abruptly slows and shifts equatorward when the drag reaches below  
234     the jet. The range of the change in jet speed and jet latitude is roughly the same as that for the  
235     global changes in boundary-layer drag. For drag changes outside of the baroclinic zone, there is  
236     relatively little change in the jet except for an increase in jet speed when the boundary-layer drag  
237     reaches the subtropics.

238     Figure 2c; d shows that the greatest changes in the zonal-mean jet speed and position in response  
239     to near-surface drag perturbations occur when the drag extends into the baroclinic zone. The  
240     change is abrupt. As the drag extends into the subtropics, there is an increase in the near-surface  
241     westerly wind speed. As a rudimentary assessment of the statistical significance consider the  
242     agreement between the statistically independent hemispheres; that is, compare the blue dot to the  
243     red dots. However, as the jet extends further poleward, the near-surface wind maximum slows to  
244     its unperturbed value followed by an abrupt reduction upon entering and crossing the baroclinic  
245     zone. The jet responses are similar if the drag started from the pole and moved equatorward.

246     The zonal-mean zonal wind response to global changes in boundary-layer drag is compared  
247     to changes in drag solely within the baroclinic zone in Figure 3. The unperturbed simulation  
248     (Figure 3) shows that the eddy-driven jet has a combined barotropic and baroclinic structure. The  
249     baroclinic part owes its existence to the north-south temperature gradient, while the barotropic  
250     component results from the action of extratropical eddies.

251 Global and baroclinic zone simulations have a similar, barotropic reduction on the poleward  
252 flank of the jet. This suggests that there has been a reduction in eddy activity on the poleward  
253 flank of the jet. Furthermore, both simulations show a baroclinic reduction in the winds between  
254 20°N/S. The baroclinic nature suggests that it might be due to enhanced eddy-momentum flux  
255 divergence within the subtropics (see Figure 4). Finally, both simulations show slight barotropic  
256 increases in the jet on the equatorward flank of the eddy-driven jet at about 40°N/S.

257 The global drag simulation shows a substantial equatorial response that is not seen in the baro-  
258 clinic zone simulation—the near-surface equatorial easterlies are substantially damped in the  
259 global drag simulation, while there is negligible change in the baroclinic zone simulation. It  
260 appears that the reduction in the subtropical jet speed is stronger in the baroclinic zone simulation.  
261 This likely occurs because there is more eddy-momentum flux divergence from the subtropics in  
262 the global drag simulations (see Figure 4). It is worth noting that while the easterlies are damped  
263 near the surface, the Hadley-circulation above the boundary layer strengthens somewhat.

264 The global-baroclinic zone difference plot in Figure 3 shows negligible extratropical barotropic  
265 differences, although the global drag simulation has a baroclinic component that is absent from  
266 the baroclinic zone simulation. Nonetheless, Figure 3 shows that the eddy-driven jet response  
267 to global variations in drag is primarily an eddy-driven jet response to variations in drag in the  
268 baroclinic zone.

269 To help understand the differences between the global and baroclinic-zone simulations Figure 4  
270 and Figure 5 show the eddy-momentum flux divergence and the meridional eddy heat fluxes for the  
271 unperturbed, baroclinic-zone simulations minus the control, global simulations minus the control,  
272 and global minus the baroclinic-zone simulations.

273 Eddy-momentum flux divergences on the flanks of the jet and eddy-momentum flux convergence  
274 into the jet are higher in the global drag simulations. In both simulations, there is an increase in

275 eddy-momentum flux convergence equatorward of the maximum in eddy-momentum flux conver-  
276 gence in the unperturbed simulation. The majority of the eddy momentum fluxes and the changes  
277 in them associated with the near-surface drag perturbations occur in the upper troposphere. Fig-  
278 ure 4 shows enhanced eddy momentum flux divergence in the subtropics in both the global and  
279 baroclinic-zone simulations.

280 The reduction of the eddy meridional heat fluxes, which are associated with baroclinic driving,  
281 on the poleward side of the jet is evident in Figure 5. This reduction occurs in both the global drag  
282 simulation and the baroclinic-zone drag simulation. The global versus baroclinic-zone difference  
283 plot shows that the reduction is identical to within 1 K m/s (Figure 5). The largest differences  
284 in the eddy meridional heat fluxes between the global and baroclinic-zone simulations occur on  
285 the equatorward flank of the jet. Because the equatorward shift of the eddy-driven jet is similar  
286 between the global and the baroclinic-zone simulations, and because the shift results from a re-  
287 duction on the poleward flank of the jet, it stands to reason that the mechanism of the eddy-driven  
288 jet shifts in response to changes in the near-surface drag is related to the suppression of baroclinic  
289 eddy driving on the poleward flank of the jet.

290 The upper-level (300 hPa) northward eddy momentum fluxes in the control simulation peak at  
291 about  $\pm 45^{\circ}\text{N}$  (Figure 6). Extratropical eddies with phase speeds between 10 and 15 m/s transport  
292 the most momentum poleward. The convergences associated with the momentum fluxes place the  
293 eddy-driven jet about 5 degrees poleward of the latitude of maximum poleward eddy momentum  
294 flux. The near-surface (850 hPa) heat/temperature fluxes also peak at about  $\pm 45^{\circ}\text{N}$ , and eddies  
295 with phase speeds between 10 and 15 m/s also transport the most heat poleward (Figure 7). The  
296 jet shifts equatorward when near-surface drag increases globally or within the baroclinic zone;  
297 however, the jet shift is greater when drag increases globally.

298     Figure 6 confirms that the eddy-driven jet shifts equatorward primarily because of reduced eddy-  
299     momentum convergence on the poleward flank of the jet. Furthermore, all eddy phase speeds  
300     contribute to the reduction of momentum convergence on the poleward flank of the jet. Moreover,  
301     the subtropical critical lines do not shift equatorward. In fact, the critical line shifts in the opposite  
302     direction of the eddy-driven jet shift in the baroclinic zone simulation, as shown by the thick green  
303     line. Hence, decreases in the eastward phase speed of equatorward propagating eddies cannot  
304     explain the equatorward shift in our simulations. The critical line on the poleward flank of the jet  
305     shifts equatorward. Therefore, the critical line appears to respond to changes in eddy momentum  
306     flux divergences rather than constrain the eddies in a causal way.

307     The differences in eddy momentum fluxes between the global and baroclinic zone simulations  
308     do not show any shifts to lower eddy phase speeds (Figure 6). There is only an anomalous dipole  
309     centered on about 40N, which implies anomalous convergence at 40N. Therefore, another mecha-  
310     nism must explain the enhanced shift in the global drag simulation. This mechanism need only to  
311     explain the equatorward shift of the eddy momentum fluxes.

312     Figure 8 shows the responses of 1) eddy-driven jet speed and latitude 2) the maximum eddy-  
313     momentum fluxes in the upper troposphere and 3) the poleward terminus of the Hadley cell<sup>2</sup> to  
314     increases in boundary-layer drag solely in one hemisphere. In these simulations, the radiative forc-  
315     ing relaxes surface temperatures to an equinox meridional profile. The Hadley cell contracts under  
316     increases in near-surface drag. The circulation response occurs solely within the drag-modified  
317     Hemisphere. The maximum eddy-momentum flux convergence reduces, which is consistent with  
318     a reduction in the eddy-driven jet speed.

---

<sup>2</sup>The Hadley cell terminus is defined as the latitude of the first zero of the meridional streamfunction that is poleward of the maximum streamfunction, evaluated at the sigma level where the maximum occurs.

319     Figure 9 shows the results of the asymmetric drag simulations with perpetual solstitial thermal  
320     profiles. Figure 9a shows the jet-speed response, while Figure 9b shows the jet-latitude response.  
321     In the figure, the subscript ‘c’ refers to control simulations, in which the boundary-layer drag is  
322     unperturbed; while the subscript ‘p’ refers to a perturbed simulation. The simulation  $Eq_c$  is forced  
323     with a perpetual equinox thermal profile.  $Eq_p$  refers to a simulation that is forced with a perpetual  
324     equinox thermal profile and within which the boundary-layer drag in the Northern Hemisphere  
325     is increased.  $So_c$  refers to a simulation that is forced with a perpetual solstice thermal profile.  
326     In contrast,  $W_p$  and  $S_p$ , although also forced with perpetual solstitial thermal profiles, refer to  
327     simulations within which drag in the winter ( $W_p$ ) and summer ( $S_p$ ) hemispheres are enhanced  
328     compared to the opposite hemisphere.

329     Figure 9 shows that there is a greater shift in the jet latitude when near-surface drag is perturbed  
330     in the summer hemisphere. This may be because the summer jet is farther poleward compared  
331     to the winter jet, and thus it simply has more space to move. In addition, the fact that the sum-  
332     mer jet is weaker and more susceptible to externally forced perturbations may also play a role.  
333     Interestingly, the magnitude of the decrease in the eddy-driven jet’s speed is greater during the  
334     winter in comparison to the summer, yet the magnitude of the jet’s equatorward shift in winter is  
335     smaller in comparison. The change in the magnitude of the eddy-driven jet is greater in winter  
336     because the magnitude of the unperturbed jet is stronger—since the meridional temperature gra-  
337     dients are stronger and because thermal-wind balance implies a directly proportional relationship  
338     between the zonal-mean zonal wind shear and the zonal-mean meridional temperature gradient  
339     within an atmospheric layer. Furthermore, it can be shown that the change in the zonal-mean  
340     zonal wind  $\Delta u_s = -0.5 u_s \Delta \ln C_D$ , if the drag parameterization is quadratic, feedbacks are ne-  
341     glected, and eddy momentum-flux convergences do not change appreciably. This results from a  
342     perturbation analysis of the steady-state, zonal-mean, vertically-averaged zonal momentum equa-

343 tion,  $\langle \partial_y \bar{u}' v' \rangle \approx C_D u_s^2$ . Therefore, one can see explicitly that changes in the magnitude of the  
344 zonal-mean zonal surface winds in response to changes in boundary-layer friction depend on the  
345 magnitude of the wind itself. Less well-understood, however, is the reason that the magnitude of  
346 the equatorward shift in winter is smaller.

347 Figure 9 confirms that there are no appreciable inter-hemispheric communication of drag  
348 changes in one hemisphere to the eddy-driven jet and storm track in the opposite hemisphere.

349 *Continent-profile drag simulations*

350 Figure 10a shows the near-surface westerly winds in the unperturbed, uniform-drag simulation  
351 ( $C_{D,L} = C_{D,O} = 0$ ). Because the simulation has no zonal asymmetries, the near-surface winds  
352 are zonally symmetric. Figure 10b shows the near-surface zonal wind response (the no-enhanced  
353 drag simulation response has been subtracted) to an imposed horizontal profile of near-surface  
354 boundary-layer drag in the shape of Earth’s continents ( $C_{D,L} \neq C_{D,O}$ ). In this control simulation,  
355 the drag over the continents is greater than over the oceans [see Table 1]. Under increases in  
356 boundary-layer drag, the eddy-driven jets in both hemispheres shift equatorward. This is consistent  
357 with previous idealized experiments with globally perturbed drag. The equatorward shift in the  
358 Northern Hemisphere is greater because the near-surface drag change is greater. The jet response  
359 in the Southern Hemisphere is more zonally symmetric than in the Northern Hemisphere because  
360 there are fewer zonal asymmetries in the boundary-layer drag profile in the Southern Hemisphere.  
361 Also, the figures suggest that idealized continental-profile boundary-layer drag helps to establish  
362 localized jets in the Northern Hemisphere (the localized near-surface winds are seen better in the  
363 contours in Figure 10c and Figure 10d). However, in our idealized simulations, the localization  
364 of the eddy-driven jet is weak, as the low-level jet remains somewhat strong over the continents.  
365 Nonetheless, this result is consistent with previous work that used idealized continents in a more

366 complex model (Brayshaw et al. 2009). In general, the eddy-driven jet speed decreases under  
367 regional increases in near-surface drag; however, regional jet speed increases are possible, as  
368 we show later. Southwest-northeast protrusions of westerly anomalies into the tropics become  
369 established off of the west coasts of North America and Africa when boundary-layer friction in  
370 the shape of the continents is introduced to a zonally symmetric friction profile.

371 Figure 10c increases the boundary-layer drag over the oceans, while the drag over the land  
372 remains fixed at the value used in the continental drag simulation (Figure 10b). The contours show  
373 the climatological wind field from the simulation shown in Figure 10b, while the color shading  
374 shows the difference from this. Figure 10c shows that jet responses are largest over the oceans  
375 and in the Southern Hemisphere. In the Southern Hemisphere, the jet shifts equatorward when the  
376 drag is increased; while in the Northern Hemisphere, the localized jets extend eastward and shift  
377 equatorward. In contrast, in Figure 10d, in which the boundary-layer friction is increased by the  
378 same amount but over the continents, the response in the Southern Hemisphere is less symmetric  
379 and weaker. Here, the Pacific jet shifts equatorward, but does not extend eastward. The Atlantic  
380 jet also shifts equatorward, however, it extends to east on the southern flank as well. In contrast to  
381 the changes in boundary-layer friction over oceans, the shifts in the jet that result from increases  
382 in friction over the land are concentrated on the western side of the Northern Hemisphere’s ocean  
383 basins.

384 Figure 10d shows that the increase in boundary-layer drag over the continents triggers a  
385 stationary-wave response that leads to a poleward shift of the jet stream over New Zealand, while  
386 an equatorward jet shift is seen to the west of South America. The eddy-driven jet’s response  
387 to enhanced boundary-layer friction over the oceans is annular mode-like, while it is stationary  
388 wave-like when perturbations are over the continents. In the Atlantic basin, the response to the

389 perturbation to the ocean boundary-layer drag has some features in common with the North At-  
390 lantic Oscillation.

391 The storm tracks, as represented by near-surface transient eddy meridional heat fluxes (Fig-  
392 ure 11), shift equatorward when the boundary-layer drag is increased. Perturbations of drag over  
393 the oceans show an annular-mode like response, while perturbations of drag over the land show  
394 a stationary wave-like response. While perturbations of drag over the land cause a clear equator-  
395 ward storm-track shift in the Northern Hemisphere, such a shift is not apparent in the Southern  
396 Hemisphere. Increasing drag over the ocean causes an equatorward storm-track shift irrespective  
397 of the hemisphere. The storm tracks and eddy-driven jet shifts are in the same sense and with  
398 similar form (Figure 10 and Figure 11). This suggests that similar mechanisms might influence  
399 their responses.

400 Drag perturbations over the ocean result in north-south jet shifts downstream of the storm tracks  
401 (Figure 10c), while perturbations over the land result in north-south jet shifts upstream of the storm  
402 tracks (Figure 10d). To understand how localized drag perturbations impact the storm tracks, ten  
403 simulations are conducted in which drag is perturbed in the baroclinic zone but in longitudinally  
404 confined regions which start at 0°E and become progressively longer in longitude until the entire  
405 baroclinic zone is perturbed.

406 The jet axis, that is the longitude profile of the maximum near-surface westerly winds, for sim-  
407 ulations varying the longitudinal extent of the baroclinic-zone drag is shown in Figure 12a. The  
408 latitude of maximum equatorward extent of the jet is a linear function of longitude until the longi-  
409 tude of the extent of drag reaches approximately 120°E, at which point the latitude of maximum  
410 equatorward extent ceases to be a function of longitude. A local maximum in equatorward ex-  
411 tent, which is a linear function of the longitudinal extent of the baroclinic-zone drag, occurs at  
412 the downstream edge of the baroclinic-zone drag rectangle. The most poleward extent of the jet

<sup>413</sup> occurs around  $10^{\circ}\text{E}$ . In simulations of low drag extent, the maximum poleward extent of the jet is  
<sup>414</sup> greater than the no-enhanced-drag case.

<sup>415</sup> The longitude profile of the jet axis suggests that the localized near-surface drag, through its  
<sup>416</sup> stationary response, exerts some control on the tilt of the jet. Figure 12a shows that the jet tilts  
<sup>417</sup> equatorward with its most northerly extent at about  $10^{\circ}\text{E}$  and its most southerly extent at the  
<sup>418</sup> smaller of two possible locations: 1) the east-most edge of the near-surface drag 2)  $100\text{-}120^{\circ}\text{E}$   
<sup>419</sup> of the west-most edge of the near-surface friction. If the baroclinic-zone drag extends beyond  
<sup>420</sup> about  $120^{\circ}\text{E}$ , then there is a modest poleward tilt of the jet axis until the east-most edge of the  
<sup>421</sup> near-surface friction. The jet axis tilts strongly poleward, that is a southwest-to-northeast tilt, east  
<sup>422</sup> of the baroclinic-zone friction.

<sup>423</sup> As the drag in the baroclinic zone extends eastward, the zonal-mean jet weakens (Figure 12b,  
<sup>424</sup> c) and shifts equatorward (Figure 12c, d). The equatorward shift of the zonal-mean jet is a linear  
<sup>425</sup> function of longitude despite the rich structure of the longitude profile of the near-surface westerly  
<sup>426</sup> wind maximum. We find a  $0.02^{\circ}$  equatorward zonal-mean jet shift per degree longitude of drag  
<sup>427</sup> extent.

<sup>428</sup> Figure 13 shows the jet speed along the jet axis. All perturbed jets attain their minimum mag-  
<sup>429</sup> nitude within roughly one baroclinic zone width east of the start of the baroclinic-zone drag. The  
<sup>430</sup> longitude of this point appears independent of the drag extent. However, the jets all attain maxi-  
<sup>431</sup> mum values east of the imposed drag. The distance east of the drag that the jets attain the maximum  
<sup>432</sup> appears to be a non-linear, decreasing function of the drag extent.

<sup>433</sup> The latitude-longitude field of near-surface westerly wind anomalies relative to the unperturbed  
<sup>434</sup> simulation is shown in Figure 14. A large portion of the jet shift is a reduction in jet speed on the  
<sup>435</sup> poleward flank of the jet. The drag extent in each figure is represented by the dashed, magenta  
<sup>436</sup> line. It is clear from the figure that the presence of the drag strip induces an equatorward jet

shift in the vicinity of the drag. East of the enhanced drag, the response is tilted; hence, the presence of localized surface drag contributes to the jet tilt in localized storm tracks. These simple block continent experiments capture the north-south jet shifts downstream of the continents seen in the realistic continent profile simulations (e.g., Figure 10a,b in the Northern Hemisphere). This suggests that the details of the shape of the continents are secondary.

The storm track response, as measured using near-surface transient eddy meridional temperature fluxes is shown in Figure 15. Poleward eddy temperature fluxes are enhanced downstream of the baroclinic-zone drag. The magnitude of the localized storm track increases as the extent of the drag increases. Within the enhanced-drag zone, eddy temperature fluxes shift equatorward, and show two maxima. This equatorward shift of the eddy temperature fluxes implies an equatorward shift of the baroclinic eddy activity. As the baroclinic stirring shifts equatorward, the zone into which upper-tropospheric eddies converge momentum also shifts equatorward. Therefore, the eddy-driven jet also shifts equatorward.

Whereas the enhanced baroclinic-zone drag adds a tilt to an otherwise zonal jet, the induced storm track is zonal. Figure 16 demonstrates that stationary eddies help create and maintain the localized storm track. Note the induced favorable and adverse near-surface meridional temperature gradients downstream and upstream of the continent. That the stationary response helps maintain a localized storm track is not surprising as the localized storm track exists only in the zonally asymmetric simulations. However, it is also apparent from the figure that enhanced baroclinicity that is independent of induced stationary temperature gradients matters. The figure shows that the idealized continent excites a wave-one stationary wave that depends on the longitudinal extent of the friction. The stationary wave is associated with a cyclone to the south of the continent and an anticyclone to the north. The net effect of the stationary-eddy fluxes is to steepen meridional temperature gradients on the eastern edge of the continent. The steepened temperature gradients then

<sup>461</sup> enhance transient eddy meridional temperature fluxes; i.e., the storm tracks, because meridional  
<sup>462</sup> eddy temperature fluxes are a strong function of meridional temperature gradients.

#### <sup>463</sup> 4. Discussion

<sup>464</sup> The global drag simulations, which cover two orders of magnitude of boundary-layer drag  
<sup>465</sup> changes, show that the eddy-driven jet shifts equatorward when boundary-layer drag is increased.  
<sup>466</sup> This agrees with previous idealized studies (Robinson 1997; Chen et al. 2007) and studies using  
<sup>467</sup> more complex models (Polichtchouk and Shepherd 2016).

<sup>468</sup> Near-surface westerly wind speed increases slightly when boundary-layer drag is increased at  
<sup>469</sup> high values of drag (Figure 1a). Although slight, the increase is statistically significant. The  
<sup>470</sup> mechanism of the increase can be understood using the theory of Robinson (2000). First, it has  
<sup>471</sup> been established that the near-surface winds are maintained by eddy convergences of westerly  
<sup>472</sup> momentum in the upper troposphere. This convergence occurs into regions where the eddies are  
<sup>473</sup> generated; that is, into their source regions. In the GCM and as found on Earth, extratropical,  
<sup>474</sup> synoptic scale eddies are primarily of baroclinic origin. Changes in baroclinicity modify the eddy  
<sup>475</sup> source region and, by extension, the region over which they converge momentum. A strong con-  
<sup>476</sup> trol of baroclinicity is the meridional temperature gradient, which is related to the vertical wind  
<sup>477</sup> shear through thermal wind balance. Increases in near-surface drag reduces near-surface winds  
<sup>478</sup> to first order. In the absence of compensating upper-tropospheric wind changes, this leads to an  
<sup>479</sup> increase in the vertical wind shear, which, under the right condition, leads to additional baroclinic  
<sup>480</sup> eddy activity, enhanced eddy momentum flux convergence, and an acceleration of the near-surface  
<sup>481</sup> winds.

<sup>482</sup> As near-surface drag enters the subtropics, the near-surface westerly wind maximum increases  
<sup>483</sup> (Figure 2c). Although several possibilities exist to explain this increase in maximum wind speed,

484 we believe that the increase results from anomalous eddy-momentum flux convergences in the  
485 upper troposphere driven by anomalous eddy driving associated with the edge of the friction im-  
486 pinging on the edge of the jet. In this context, the anomalous eddy activity may result from  
487 barotropic instability or from the north-south gradient in boundary-layer friction interacting with  
488 the background winds. That the increase in jet speed vanishes as the extent of the surface drag  
489 moves further poleward serves as evidence that the increase is edge related.

490 Comparing the global and baroclinic-zone drag simulations, Figure 3 shows that the response of  
491 the eddy-driven jet to global increases in drag are captured by varying drag solely in the baroclinic  
492 zone. Global variations of drag introduces additional responses which appear confined to the  
493 equatorial and polar regions for the most part. Therefore in addressing model biases in the eddy-  
494 driven jet, particular attention should be paid to drag parameterizations in the vicinity of the jet  
495 itself.

496 It is clear from figure 3 that the jet shift results from a barotropic reduction of the zonal winds  
497 on the poleward side of the eddy-driven jet. This implies a reduction in the eddy-momentum flux  
498 convergence in that region.

499 Our results agree with prior work that suggests that eddy dynamics on the poleward flank of the  
500 jet are more important for the eddy-driven jet shift in response to changes in near-surface drag  
501 (Lorenz 2014), in contrast to the idea that subtropical dynamics are primarily responsible for the  
502 shift (Chen et al. 2007).

503 We find that the phase speeds of eddies with the largest near-surface heat flux are also the phase  
504 speeds at which upper-tropospheric eddies transport the largest amount of momentum. Poleward  
505 eddy heat fluxes—largely the product of baroclinic instability—are associated with upward fluxes  
506 of wave activity, which in turn excite upper-tropospheric, equatorward-propagating Rossby waves.  
507 These Rossby waves converge momentum into the region of their excitation. The similarity of

508 phase speeds appears analogous to the frequency of the forcing equaling the frequency of the  
509 response in a simple forced harmonic system.

510 Because extrema in the near-surface heat flux spectra shift equatorward in tandem with the eddy-  
511 driven jet when drag is perturbed globally and in the baroclinic zone, it is possible that shifts in  
512 the baroclinic stirring explain the eddy-driven jet shift. Therefore, we hypothesize that changes in  
513 the baroclinic driving causally shifts the jets in our simulations.

514 The equinox, hemispherically asymmetric simulations (Figure 8) show that changes in drag in  
515 one hemisphere are balanced by circulation responses in the forced hemisphere with relatively  
516 little extratropical response in the opposite hemisphere. This may be in contrast to simulations in  
517 moist climates in which moisture responses may enhance linkages between opposite hemispheres  
518 (Polichtchouk and Shepherd 2016).

519 The near-surface protrusion of westerlies into the tropics off the west coasts of North America  
520 and North Africa is caused by the land-sea friction contrast. Compare the contours in Figure 10a  
521 and Figure 10b to see this effect. This protrusion is important because it may facilitate Rossby  
522 wave propagation into midlatitudes. Wave guides are zonal bands of upper-level westerly winds.  
523 They enable meridional propagation of Rossby waves. Upper-level tropical divergences, forced,  
524 for example, by tropical convection, generate Rossby waves that could propagate into the extrat-  
525ropics along these waveguides and influence extratropical variability (Hoskins and Karoly 1981;  
526 Hoskins and Ambrizzi 1993; Ambrizzi and Hoskins 1997). One of the stationary responses to in-  
527 creases in near-surface drag (see Figure 16) is a westerly wind anomaly on the equatorward flank  
528 of the continent. Furthermore, because surface drag is balanced by column-integrated eddy mo-  
529 mentum flux convergences, enhanced near-surface drag forces eddy-momentum flux convergences  
530 aloft and accelerates the westerlies. Thus, these two effects suggest that the surface drag associated  
531 with continents in the vicinity of the subtropics extends westerlies anomalously equatorward, shift-

532 ing the waveguides closer to the regions of tropical convection. Hence, the subtropical continents  
533 could play an important role in tropical-extratropical teleconnections. This provides an additional  
534 reason why it is important for climate and forecast models to get the location and intensity of  
535 boundary-layer drag correct.

536 Increasing drag over the oceans in the Northern Hemisphere leads to an eastward extension of  
537 the weakly localized Atlantic and Pacific jets. These localized jets occur on the western edge of  
538 the Pacific and Atlantic oceans (contours in Figure 10c), and the strongest jet shifts occur at the  
539 eastern edge of the enhanced drag region (Figure 12a and Figure 14) largely because of enhanced  
540 stationary eddy fluxes (Figure 16). The combined effect manifests as an extension of the eastern  
541 edge of the localized jet.

542 Increasing drag globally shifts the eddy-driven jet equatorward, in agreement with previous  
543 studies. It is also in agreement with the results from studies using the less realistic, Rayleigh  
544 friction parameterizations in their simulations; i.e. linear drag.

545 We find that despite the linear decrease in latitude of the zonal-mean jet maximum with in-  
546 creasing longitude extent of baroclinic-zone drag, the zonal profile of wind in the sector drag  
547 experiments exhibits a rich structure and may even show a local poleward shift of the jet axis.  
548 Local near-surface drag was also found to influence the jet-axis tilt.

549 The gradually increasing boundary-layer drag in the meridional direction shifted the eddy-driven  
550 jet equatorward only after the drag reaches in the vicinity of the jet; yet, when the friction reached  
551 the jet, the equatorward jet shift was similar in magnitude to the shifts seen when drag was in-  
552 creased globally. Increasing the drag starting at the pole and moving toward the equator (not  
553 shown) also yields an abrupt transition when the drag reaches under the jet. Because a large pro-  
554 portion of the overall jet shift occurs when the boundary-layer drag crosses under the jet, and be-  
555 cause the response is independent of the direction from which the boundary-layer drag approaches

556 prior to crossing the jet, the principal mechanism controlling the jet shift is likely to be local in dry  
557 models.

558 The hemispherically-asymmetric simulations show that variations in drag in one hemisphere  
559 have negligible effects in the opposite hemisphere. Therefore, and consistent with the interpreta-  
560 tion of Polichtchouk and Shepherd (2016), moist dynamics and ocean dynamics likely account for  
561 any cross equatorial effects observed in more complex models. Nonetheless, these results suggest  
562 that biases in the dry part of the dynamics may be addressed in a hemispherically independent  
563 way. That is, one can adjust drag in one hemisphere without adversely affecting the other through  
564 dry dynamical responses.

565 We showed that stationary eddies help localize extratropical storm tracks. This is not a new re-  
566 sult (Chang et al. 2002; Kaspi and Schneider 2013). But here, localization is demonstrated in the  
567 absence of orography and diabatic heat sources. What is new is the natural extension of the results  
568 contained herein that suggests that the stationary eddies associated with a downstream continent  
569 help terminate an upstream storm track by creating an unfavorable meridional temperature gra-  
570 dient through stationary-eddy temperature fluxes (see Figure 16). Hence, the European continent  
571 helps terminate the Atlantic storm track not only though stationary eddies generated by the storm  
572 track itself (Kaspi and Schneider 2013), or from the direct mechanically forced dissipation (Chang  
573 et al. 2002), but also through the drag induced stationary-wave fluxes associated with the conti-  
574 nent. The same is true of the adverse effect of the American continent on the Pacific storm track.  
575 This result complements recent work, which finds that near-surface drag modulates circulation  
576 responses through stationary wave interactions (van Niekerk et al. 2017).

577 *Theory of eddy-driven jet shifts in response to boundary layer drag*

578 Drag, a non-conservative force, does negative work on a fluid parcel. Sources of drag in Earth's  
 579 atmosphere include skin friction at the surface, form drag associated with a flow impinging on  
 580 topography, and momentum transfer associated with macroturbulence and breaking waves. The  
 581 applicable physical law is the conservation of angular momentum. The zonal angular momentum  
 582  $l$  of a fluid parcel consists of two parts, the part due to Earth's solid body rotation and the part due  
 583 to the parcel's relative motion:

$$l = \Omega (a \cos \varphi)^2 + u a \cos \varphi, \quad (4)$$

584 where  $a$  is the mean radius of Earth,  $\varphi$  is latitude, and  $\Omega$  is Earth's angular velocity.

585 *a. The angular momentum conserving case*

586 Insight into the expected shifts of tropospheric jets due to changes in zonal wind speed in a ro-  
 587 tating frame can be obtained by considering the angular momentum conserving case. It is apparent  
 588 from Equation 4 that  $l = l(u, \varphi)$ , if  $a$  and  $\Omega$  are considered parameters.

589 In the absence of torques on a system,  $l$  is conserved, which implies that,

$$\Delta l = 0 = \partial_u l \Delta u + \partial_\varphi l \Delta \varphi \quad (5)$$

590 From Equation 4, we have that  $\partial_u l = a \cos \varphi$  and  $\partial_\varphi l = -a \sin \varphi (2\Omega a \cos \varphi + u)$ . In this angular  
 591 momentum conserving regime, a simple relation emerges for changes in the latitude of a fluid  
 592 parcel immediately following an externally forced change to its zonal wind speed:

$$\Delta \varphi = -\frac{\partial_u l}{\partial_\varphi l} \Delta u \quad (6)$$

$$\Delta \varphi = \frac{\cot \varphi}{2\Omega a \cos \varphi + u} \Delta u \quad (7)$$

593 Equation 7 suggests that a fluid parcel will shift poleward for externally forced increases in its  
 594 zonal wind speed and equatorward for externally forced decreases in its zonal wind speed. Fig-  
 595 ure 17 shows the increase in a fluid parcel's latitude for a 1 m/s increase in its zonal wind speed, if  
 596 it conserves its angular momentum. It is clear from the figure that the parcel's increase in latitude is  
 597 everywhere directly proportional to the externally-forced increase in zonal wind speed. However,  
 598 the sensitivity to increases in zonal wind speed is a decreasing function of latitude. These results  
 599 are consistent with our expectations because changes in angular momentum depend on changes in  
 600 the perpendicular distance to Earth's axis of rotation and because larger changes in latitude are re-  
 601 quired at lower latitudes for equal changes in the perpendicular distance to Earth's axis of rotation  
 602 than at higher latitudes. Whereas this simple analysis presents a useful indication of how the lati-  
 603 tude of jets could change as the wind speed changes in the absence of torques on the fluid parcel,  
 604 it is inadequate for explaining changes in the eddy-driven jet since drag plays an important role  
 605 and since angular momentum is not conserved in midlatitudes in the presence of macroturbulence.  
 606 Furthermore, the analysis predicts enhanced sensitivities on the equatorward flank of the jet, while  
 607 our simulations show enhanced sensitivities on the poleward flank of the jet.

### 608 *b. The non-conservative force case*

609 Because the effects of surface drag are of interest, we start with the near-surface zonal-mean  
 610 zonal momentum equation within the baroclinic zone.

$$f\bar{v} = \partial_y (\bar{u}\bar{v} + \bar{u}'\bar{v}') + \partial_p (\bar{u}\bar{w} + \bar{u}'\bar{w}'), \quad (8)$$

611 where the overline represents a time and zonal mean, and the prime represents a departure from a  
 612 temporal mean. Near to the surface, the mean northward flux of westerly momentum by transient  
 613 eddies is negligible (Ait-Chaalal and Schneider 2015) [see also Figure 4]. Within the baroclinic

614 zone, the mean meridional circulation is the thermally indirect, eddy-driven Ferrel cell. If, fol-  
 615 lowing Schneider and Bordoni (2008), one considers the interior of the baroclinic zone, where  
 616 the surface streamlines are approximately horizontal, then one may neglect vertical momentum  
 617 transports by the mean meridional circulation. Combined, these assumptions reduce the zonal  
 618 momentum equation to

$$(1 - \text{Ro}) f \bar{v} = \tau u, \quad (9)$$

619 where  $\text{Ro} = \partial_y \bar{u} / f$  is the local Rossby number. Here, we model near-surface vertical eddy-  
 620 momentum flux divergences as a linear drag, for expository purposes. Here  $\tau^{-1}$  is the drag time  
 621 scale.

622 The zonal-mean meridional momentum equation within the baroclinic zone is given by,

$$-f \bar{u} - \partial_y \bar{\Phi} = \partial_y (\bar{v}^2 + \bar{v}'^2) + \partial_p (\bar{v} \bar{w} + \bar{v}' \bar{w}'), \quad (10)$$

623 where  $\bar{\Phi}$  is the time and zonal-mean geopotential. Similarly, the zonal-mean meridional momen-  
 624 tum equation reduces to,

$$(1 - \text{Ro}) f \bar{u} = -\tau v - \partial_y \bar{B}, \quad (11)$$

625 where  $B = \bar{\Phi} + 0.5 (\bar{u}^2 + \bar{v}^2)$  is the Bernoulli function. Hence, we have a system of equations  
 626 (Equation 9 and Equation 11) that we solve, treating the gradient of the Bernoulli function as a  
 627 parameter:

$$\bar{u} = -\frac{(1 - \text{Ro}) f \partial_y \bar{B}}{f^2(1 - \text{Ro})^2 + \tau^2} \quad (12)$$

$$\bar{v} = -\frac{\tau \partial_y \bar{B}}{f^2(1 - \text{Ro})^2 + \tau^2} \quad (13)$$

628

629 We note that these equations are the same ones derived in Schneider and Bordoni (2008). The  
 630 partial derivative of the equations of  $\bar{u}$  and  $\bar{v}$  gives one measure of the sensitivity of the zonal mean

winds to linear drag. The sensitivities can be used to ascertain whether the asymmetries in the zonal-mean wind's response to changes in drag result from the zonal profile of the components of the sensitivities. The drag sensitivities are found to be,

$$\delta\bar{u}_\tau = \partial_y B \frac{2\tau f(1 - Ro)}{(f^2(1 - Ro)^2 + \tau^2)^2} \delta\tau \quad (14)$$

$$\delta\bar{v}_\tau = -\partial_y B \frac{f^2(1 - Ro)^2 - \tau^2}{(f^2(1 - Ro)^2 + \tau^2)^2} \delta\tau \quad (15)$$

634

First, observe that the limit of the sensitivities as the Coriolis parameter gets large is zero. Bearing in mind that in midlatitudes  $Ro \ll 1$ , it becomes clear that Earth's curvature does not explain the enhanced reduction of  $\bar{u}$  on the poleward flank of the jet as drag increases uniformly in the baroclinic zone. Indeed, because  $f$  is a monotonically increasing function of latitude and because the sensitivities are inversely proportional to  $f$ , higher latitudes will experience lower sensitivities to changes in drag, which is contrary to our observations.

Since the near-surface drag in our simulations is a constant function of latitude within the baroclinic zone, we turn our attention to the zonal-mean meridional profile of the Bernoulli function. Figure 18 plots the Bernoulli function and its components for the control simulation. The gradient of the Bernoulli function is predominantly negative and dominated by the geopotential term. The geopotential-gradient is asymmetric about the jet core: it is less negative on the equatorward flank of the jet. The mean kinetic energy gradient is also asymmetric about the jet maximum, it changes sign. The sense of these asymmetries enhances the sensitivity of the zonal-mean zonal wind to changes in near-surface drag on the poleward flank of the jet, while it reduces the sensitivity on the equatorward flank. Indeed, the meridional profile of drag sensitivity, which is dominated by the Bernoulli function, explains why the jet response to changes in drag is asymmetric about the jet core. The sensitivities associated with the gradient in the mean kinetic energy enhances the

asymmetry in the sensitivity, but it is secondary to the asymmetry associated with the gradient of the geopotential.

Therefore, the equatorward shift in the eddy-driven jet results from a contraction on the poleward flank of the baroclinic zone. The contraction on the poleward flank of the jet may sometimes be accompanied by an equatorward jet expansion. These changes in the baroclinic zone are driven primarily by the profile of the Bernoulli function, which is asymmetric about the storm tracks and eddy-driven jet.

## 5. Conclusion

Novel simulations were conducted in a dry, idealized general circulation model (GCM). These simulations provide new insight into the eddy-driven jet dynamics in response to changes in near-surface drag and a new, rich array of case studies against which to test theories of jet and storm-track shifts.

By perturbing the near-surface drag in a zonal band in the vicinity of the eddy-driven jet, we demonstrated that much of the jet response to global variations in surface drag are captured by perturbing the drag locally about the climatological jet.

Hemispherically asymmetric near-surface drag simulations were conducted to probe possible inter-hemispheric dynamical interactions. However, it was found that perturbing drag in one hemisphere had negligible effect on the eddy-driven jet in the opposite hemisphere. This remained true when the simulations were run in perpetual summer and winter configurations. This suggests that it is possible to adjust drag in one hemisphere without substantially affecting the jet in the opposite hemisphere through dry dynamics.

The eddy-driven jet latitude was found to be more sensitive to variations in near-surface drag in summer than in winter; while, the wintertime eddy-driven jet strength was more sensitive to

675 perturbations in near-surface drag. It was shown that there was a larger change in jet speed in  
676 winter because the jet speeds are higher in winter. Furthermore, it was shown that asymmetries in  
677 the Bernoulli function explain the asymmetric reduction in the jet speed around the core, which  
678 resulted in an equatorward contraction of the jet when near-surface drag increases.

679 It is found that zonally localized drag sets up a localized storm track and a tilted jet downstream.  
680 Furthermore, it was demonstrated that differential variations in land versus ocean drag can modify  
681 the tilt of the Atlantic and Pacific jets.

682 Finally, it is suggested that the near-surface drag associated with Earth-like continents facilitates  
683 tropical-extratropical teleconnections by modifying subtropical waveguides. Thus, climate and  
684 forecast models have additional reasons to better constrain their drag parameterizations, especially  
685 in the subtropics and extratropics.

686 The results contained herein demonstrate that further research into the fundamentals of eddy-  
687 driven jet dynamics is warranted and that scope exists for advancing our understanding of it in  
688 order to improve climate and forecast models.

689 *Acknowledgments.* This work was conducted as part of the summerTIME project and was funded  
690 through the NERC grant #NE/M005887/1. We thank the reviewers for their helpful comments on  
691 the original manuscript.

## 692 **References**

- 693 Ait-Chaalal, F., and T. Schneider, 2015: Why eddy momentum fluxes are concentrated in the upper  
694 troposphere. *Journal of the Atmospheric Sciences*, **72**, 1585–1604.
- 695 Ambrizzi, T., and B. J. Hoskins, 1997: Stationary rossby-wave propagation in a baroclinic at-  
696 mosphere. *Quarterly Journal of the Royal Meteorological Society*, **123 (540)**, 919–928, doi:

- 697 10.1002/qj.49712354007.
- 698 Baker, H., T. Woollings, and C. Mbengue, 2017: Eddy-driven jet sensitivity to diabatic heating in  
699 an idealized gcm. *Journal of Climate*, **0**, doi:<https://doi.org/10.1175/JCLI-D-16-0864.1>.
- 700 Barnes, E. A., and D. L. Hartmann, 2011: Rossby wave scales, propagation, and the variability  
701 of eddy-driven jets. *Journal of the Atmospheric Sciences*, **68** (12), 2893–2908, doi:[10.1175/JAS-D-11-039.1](https://doi.org/10.1175/JAS-D-11-039.1).
- 703 Barnes, E. A., D. L. Hartmann, D. M. W. Frierson, and J. Kidston, 2010: Effect of latitude on the  
704 persistence of eddy-driven jets. *Geophysical Research Letters*, **37** (11), n/a–n/a, doi:[10.1029/2010GL043199](https://doi.org/10.1029/2010GL043199), URL <http://dx.doi.org/10.1029/2010GL043199>, 111804.
- 706 Brayshaw, D., B. Hoskins, and M. Blackburn, 2008: The storm-track response to idealized SST  
707 perturbations in an aqua-planet GCM. *Journal of the Atmospheric Sciences*, **65**, 2842–2860.
- 708 Brayshaw, D. J., B. Hoskins, and M. Blackburn, 2009: The basic ingredients of the North Atlantic  
709 storm track. Part I: land-sea contrast and orography. *Journal of the Atmospheric Sciences*, **66**,  
710 2539–2558.
- 711 Chang, E., S. Lee, and K. Swanson, 2002: Storm track dynamics. *Journal of Climate*, **15**, 2163–  
712 2183.
- 713 Charney, J. G., 1947: The dynamics of long waves in a baroclinic westerly current. *Journal of*  
714 *Meteorology*, **4** (5), 135–162.
- 715 Chen, G., I. M. Held, and W. A. Robinson, 2007: Sensitivity of the latitude of the surface westerlies  
716 to surface friction. *Journal of the Atmospheric Sciences*, **64**, 2899–2915.
- 717 Eady, E. T., 1949: Long waves and cyclone waves. *Tellus*, **1**, 33–52.

- 718 Hayashi, Y., 1971: A generalized method of resolving disturbances into progressive and retro-  
719 gressive waves by space Fourier and time cross-spectral analysis. *J. Met. Soc. Japan*, **49** (2),  
720 125–128.
- 721 Held, I. M., and M. J. Suarez, 1994: A proposal for the intercomparison of the dynamical cores  
722 of atmospheric general circulation models. *Bulletin of the American Meteorological Society*,  
723 **75** (10), 1825–1830, doi:10.1175/1520-0477(1994)075<1825:APFTIO>2.0.CO;2.
- 724 Hoskins, B. J., and T. Ambrizzi, 1993: Rossby wave propagation on a realistic longitudi-  
725 nally varying flow. *Journal of the Atmospheric Sciences*, **50** (12), 1661–1671, doi:10.1175/  
726 1520-0469(1993)050<1661:RWPOAR>2.0.CO;2.
- 727 Hoskins, B. J., and D. J. Karoly, 1981: The steady linear response of a spherical atmosphere  
728 to thermal and orographic forcing. *Journal of the Atmospheric Sciences*, **38** (6), 1179–1196,  
729 doi:10.1175/1520-0469(1981)038<1179:TSLROA>2.0.CO;2.
- 730 James, I., 1987: Suppression of baroclinic instability in horizontally sheared flows. *Journal of the*  
731 *Atmospheric Sciences*, **44** (24), 3710–3720.
- 732 James, I. N., and L. J. Gray, 1986: Concerning the effect of surface drag on the circulation of a  
733 baroclinic planetary atmosphere. *Quarterly Journal of the Royal Meteorological Society*, **112**,  
734 1231–1250.
- 735 Kaspi, Y., and T. Schneider, 2013: The role of stationary eddies in shaping midlatitude storm  
736 tracks. *Journal of the Atmospheric Sciences*, **70**, 2596–2613.
- 737 Kidston, J., and G. K. Vallis, 2010: Relationship between eddydriven jet latitude and width.

- 738 Kidston, J., and G. K. Vallis, 2012: The relationship between the speed and the latitude of an  
739 eddy-driven jet in a stirred barotropic model. *Journal of the Atmospheric Sciences*, **69** (11),  
740 3251–3263, doi:10.1175/JAS-D-11-0300.1.
- 741 Lorenz, D. J., 2014: Understanding midlatitude jet variability and change using Rossby wave  
742 chromatography: wave-mean flow interaction. *Journal of the Atmospheric Sciences*, **71**, 3684–  
743 3705.
- 744 Lorenz, E., 1955: Available potential energy and the maintenance of the general circulation. *Tellus*,  
745 **VII** (2), 157–167.
- 746 Mbengue, C., and T. Schneider, 2013: Storm track shifts under climate change: what can be  
747 learned from large-scale dry dynamics. *Journal of Climate*, **26**, 9923–9930.
- 748 Mbengue, C., and T. Schneider, 2017: Storm-track shifts under climate change: toward a mech-  
749 anistic understanding using baroclinic mean available potential energy. *Journal of the At-*  
750 *mospheric Sciences*, 93–110, doi:10.1175/JAS-D-15-0267.1, URL <http://dx.doi.org/10.1175/JAS-D-15-0267.1>.
- 752 Mbengue, C., and T. Schneider, 2018: Linking hadley circulation and storm tracks in a conceptual  
753 model of the atmospheric energy balance. *Journal of the Atmospheric Sciences*, submitted, doi:  
754 10.1175/JAS-D-17-0098.1.
- 755 Phillips, N., 1956: The general circulation of the atmosphere: a numerical experiment. *Quarterly*  
756 *Journal of the Royal Meteorological Society*, **82** (352), 123–164.
- 757 Pithan, F., T. G. Shepherd, G. Zappa, and I. Sandu, 2016: Climate model biases in jet streams,  
758 blocking and storm tracks resulting from missing orographic drag. *Geophysical Research Let-*  
759 *ters*, **43** (13), 7231–7240, doi:10.1002/2016GL069551, 2016GL069551.

- 760 Polichtchouk, I., and T. G. Shepherd, 2016: Zonal-mean circulation response to reduced air-sea  
761 momentum roughness. *Quarterly Journal of the Royal Meteorological Society*, **142** (700), 2611–  
762 2622.
- 763 Randel, W. J., and I. M. Held, 1991: Phase speed spectra of transient eddy fluxes and crit-  
764 ical layer absorption. *Journal of the Atmospheric Sciences*, **48** (5), 688–697, doi:10.1175/  
765 1520-0469(1991)048<688:PSSOTE>2.0.CO;2.
- 766 Robinson, W. A., 1997: Dissipation dependence of the jet latitude. *Journal of Climate*, **10** (2),  
767 176–182, doi:10.1175/1520-0442(1997)010<0176:DDOTJL>2.0.CO;2.
- 768 Robinson, W. A., 2000: A baroclinic mechanism for the eddy feedback on the zonal index.  
769 *Journal of the Atmospheric Sciences*, **57** (3), 415–422, doi:10.1175/1520-0469(2000)057<0415:  
770 ABMFTE>2.0.CO;2.
- 771 Sandu, I., P. Bechtold, and Others, 2016: Impacts of parameterized orographic drag on the  
772 northern hemisphere winter circulation. *J. Adv. Model. Earth Syst.*, **8** (1), 196–211, doi:  
773 10.1002/2015MS000564.
- 774 Schneider, T., 2004: The tropopause and the thermal stratification in the extratropics of a dry  
775 atmosphere. *Journal of the Atmospheric Sciences*, **61**, 1317–1340.
- 776 Schneider, T., and S. Bordoni, 2008: Eddy-mediated regime transitions in the seasonal cycle of  
777 a Hadley circulation and implications for monsoon dynamics. *Journal of the Atmospheric Sci-  
778 ences*, **65**, 915–934.
- 779 Schneider, T., and C. Walker, 2006: Self-organization of atmospheric macroturbulence into critical  
780 states of weak nonlinear eddy-eddy interactions. *Journal of the Atmospheric Sciences*, **63**, 1569–  
781 1586.

- 782 Stephenson, D. B., 1994: The northern hemisphere tropospheric response to changes in the  
783 gravity-wave drag scheme in a perpetual January GCM. *Quarterly Journal of the Royal Me-*  
784 *teorological Society*, **120** (517), 699–712, doi:10.1002/qj.49712051709, URL <http://dx.doi.org/10.1002/qj.49712051709>.
- 785
- 786 Stephenson, D. B., 1995: The impact of changing the horizontal diffusion scheme on the northern  
787 winter climatology of a general circulation model. *Quarterly Journal of the Royal Meteorologi-*  
788 *cal Society*, **121** (521), 211–226, doi:10.1002/qj.49712152110, URL <http://dx.doi.org/10.1002/qj.49712152110>.
- 789
- 790 van Niekerk, A., J. F. Scinocca, and T. G. Shepherd, 2017: The modulation of stationary waves,  
791 and their response to climate change, by parameterized orographic drag. *Journal of the Atmo-*  
792 *spheric Sciences*, **74** (8), 2557–2574, doi:10.1175/JAS-D-17-0085.1.
- 793
- 794 Woollings, T., A. Hannachi, and B. Hoskins, 2010: Variability of the north atlantic eddy-driven  
795 jet stream. *Quarterly Journal of the Royal Meteorological Society*, **136** (649), 856–868, doi:  
796 10.1002/qj.625.
- 797
- 798 Yin, J., 2005: A consistent poleward shift of the storm track in simulations of 21st-century climate.  
799 *Geophysical Research Letters*, **32**, L18 701, doi:10.1029/2005GL023 684.

798 **LIST OF TABLES**

799 <b>Table 1.</b>	Continental-profile simulations. The enhanced drag coefficients are in units of	40
800 $10^{-7} \text{ m}^{-1}$ .	.	.

TABLE 1. Continental-profile simulations. The enhanced drag coefficients are in units of  $10^{-7} \text{ m}^{-1}$ . ‘O’ represents ocean while ‘L’ represents land.

	<i>No Enhanced Drag</i>	<i>Ctrl</i>	<i>Oexp</i>	<i>Lexp</i>
$C_{D,O}$	0.0	4.0	16.0	4.0
$C_{D,L}$	0.0	32.0	32.0	44.0

801 LIST OF FIGURES

- Fig. 1.** The eddy-driven jet speed (a) and latitude (b) response to global drag variations. The eddy-driven jet is measured using zonal-mean zonal winds averaged between  $\sigma = 0.8$  and  $\sigma = 0.6$ . The blue dots show the southern hemisphere, while the red dots show the statistically-independent northern hemisphere. The error bars show the 95% confidence interval about the jet's mean speed and latitude. . . . . 44

**Fig. 2.** The eddy-driven jet speed (a, c) and latitude (b, d) response to boundary-layer drag. (a, b): jet response to changes in boundary-layer drag within the baroclinic zone, the constant-width region between 35 N/S and 55 N/S. (c, d): jet response to near-surface drag that extends from the equator to the latitude specified on the abscissa. The eddy-driven jet is defined using the zonal-mean zonal winds averaged between  $\sigma = 0.8$  and  $\sigma = 0.6$ . The blue dots show the Southern Hemisphere, while the red dots show the statistically-independent Northern Hemisphere. . . . . 45

**Fig. 3.** The latitude-sigma zonal-mean zonal wind field for 1) a control simulation with unperturbed near-surface drag 2) the globally enhanced near-surface drag simulation minus the control simulation 3) the enhanced near-surface drag within the baroclinic zone simulation minus the control simulation and 4) the globally enhanced drag simulation minus drag enhanced within the baroclinic zone simulation. The baroclinic zone is the axisymmetric region between  $\pm 35^\circ\text{N}$  and  $\pm 55^\circ\text{N}$ . The black, unfilled contours, save for those in one panel, show the zonal-mean zonal wind field in the control simulation. The enhanced drag value used in the perturbed simulations is  $64 \times 10^{-7} \text{ m}^{-1}$ . . . . . 46

**Fig. 4.** The latitude-sigma eddy momentum flux divergence  $\partial_\phi (\overline{u'v'} \cos \phi) / (R \cos \phi)$  field for 1) a control simulation with no enhanced near-surface drag 2) the globally enhanced near-surface drag simulation minus the control simulation 3) the near-surface drag enhanced in the baroclinic zone simulation minus the control simulation and 4) the globally enhanced drag simulation minus the drag enhanced in the baroclinic zone simulation. The baroclinic zone is the axisymmetric region between  $\pm 35^\circ\text{N}$  and  $\pm 55^\circ\text{N}$ . The black, unfilled contours, save for those in one panel, show the field of eddy momentum flux divergence in the control simulation. We have multiplied by the constant radius of Earth to obtain units of  $\text{m}^2/\text{s}^2$ . . . . . 47

**Fig. 5.** The latitude-sigma meridional eddy heat fluxes  $\overline{v'\theta'}$  field for 1) a control simulation with no enhanced near-surface drag 2) the globally enhanced near-surface drag simulation minus the control simulation 3) the near-surface drag enhanced in the baroclinic zone simulation minus the control simulation and 4) the globally enhanced drag simulation minus drag enhanced in the baroclinic zone simulation. The baroclinic zone is the axisymmetric region between  $\pm 35^\circ\text{N}$  and  $\pm 55^\circ\text{N}$ . The black, unfilled contours, save for those in one panel, show the field of eddy heat fluxes in the control simulation. . . . . 48

**Fig. 6.** The contours in the control simulation show the phase-speed spectrum of upper-level (300 hPa) northward momentum fluxes. The thick gray line in the control simulation shows the meridional profile of the upper-level westerly wind, which has been normalized by the cosine of latitude. The contours in the remaining plots show differences in the northward momentum fluxes. The thick green lines show the normalized westerly wind in the perturbed simulations. The thin lines bounding the westerlies are twice the standard error of a 30-member ensemble mean. . . . . 49

**Fig. 7.** The contours in the control simulation show the phase-speed spectrum of near-surface (850 hPa) northward temperature fluxes. The thick gray line in the control simulation shows the meridional profile of the near-surface westerly wind, which has been normalized by

847 the cosine of latitude. The contours in the remaining plots show differences in the north-  
848 ward temperature fluxes. The thick green lines show the normalized westerly wind in the  
849 perturbed simulations. The thin lines bounding the westerlies are twice the standard error  
850 of a 30-member ensemble mean. The thin horizontal lines mark the Northern Hemisphere  
851 westerly wind maximum. . . . .

50

852 **Fig. 8.** The jet-speed (a), jet-latitude (b), vertically-averaged eddy momentum fluxes (c), and the  
853 Hadley cell terminus latitude (d) responses to variations in boundary-layer drag in the South-  
854 ern Hemisphere. The blue dots show values for the Southern Hemisphere, while the red dots  
855 show values for the Northern Hemisphere. The error bars are computed using a boot-strap  
856 procedure. . . . .

51

857 **Fig. 9.** Jet speed (a) and latitude (b) for three simulations in which boundary-layer friction is per-  
858 turbed, one unperturbed equinox control simulation  $Eq_c$ , and one unperturbed solstice con-  
859 trol simulation  $So_c$ .  $Eq_p$  shows jet speed and latitude for increased near-surface friction  
860 in the hemisphere indicated in red in an equinox profile;  $W_p$  shows the two metrics for in-  
861 creased near-surface friction in the winter hemisphere; while  $S_p$  shows it for the summer  
862 hemisphere. In the solstice profile simulations, the blue dots show the winter hemisphere,  
863 while the red dots show the summer hemisphere. The error bars show a 95% confidence  
864 interval for the mean. . . . .

52

865 **Fig. 10.** Near-surface zonal wind response to variations in boundary-layer drag. a: Near-surface  
866 zonal winds in the no enhanced drag simulation. b: The Earth-like boundary-layer drag sim-  
867 ulation minus the no enhanced drag simulation (filled, colored contours) and the near-surface  
868 zonal winds from the no enhanced drag simulation (grey, unfilled contours). c: Enhanced  
869 drag over the oceans simulation minus the Earth-like boundary-layer drag simulation (filled,  
870 colored contours) and the near-surface zonal winds from the Earth-like boundary-layer drag  
871 simulation (gray, unfilled contours). d: Enhanced drag over the land simulation minus the  
872 Earth-like boundary-layer drag simulation (filled, colored contours) and the near-surface  
873 zonal winds from the Earth-like boundary-layer drag simulation (gray, unfilled contours). . . . .

53

874 **Fig. 11.** Similar to Fig. 10., but for the storm-track response to variations in boundary-layer drag.  
875 The storm track is identified using near-surface meridional eddy heat fluxes  $\sqrt{\theta'}$ . . . . .

54

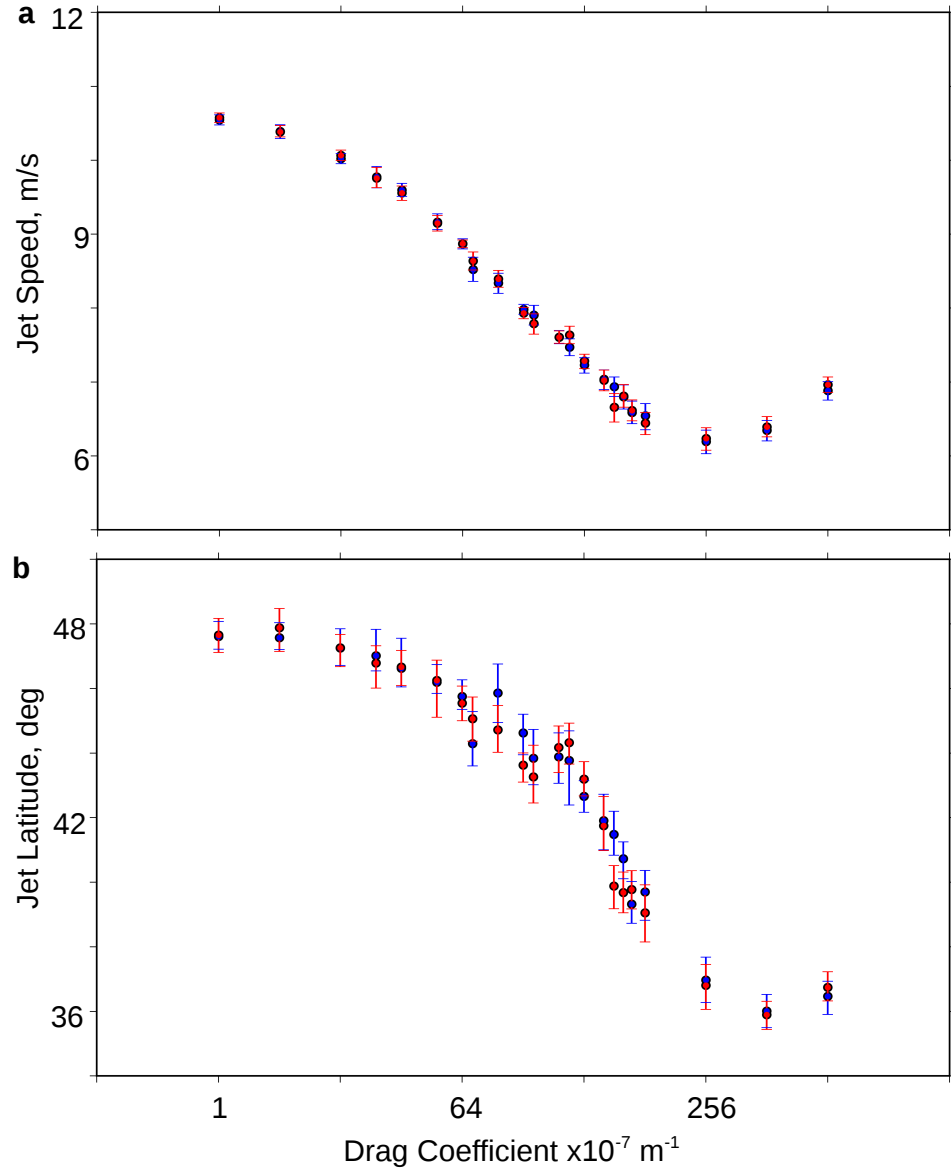
876 **Fig. 12.** a: Longitude profiles of the extremum of the near-surface zonal wind (the jet axis) for sim-  
877 ulations in which the longitudinal extent of the near-surface drag within the baroclinic zone  
878 is enhanced relative to the rest of the globe. The dashed-vertical lines denote the drag ex-  
879 tent for jet axis profiles of same color. The black lines show the no enhancement and the  
880 axisymmetric enhancement cases. b: The zonal-mean jet speed response to increases in the  
881 longitudinal extent of near-surface drag. The dashed, red curve shows a non-linear fit to the  
882 GCM's output. c: The near-surface zonal-mean zonal wind profile response to changes in  
883 the longitudinal extent of near-surface baroclinic zone drag. The star indicates the computed  
884 location of the jet. The color scheme is that same as in Fig. 10a. d: The zonal-mean jet lat-  
885 itude response to increases in the longitudinal extent of near-surface drag. The dashed, red  
886 line shows a linear fit to the GCM's output. . . . .

55

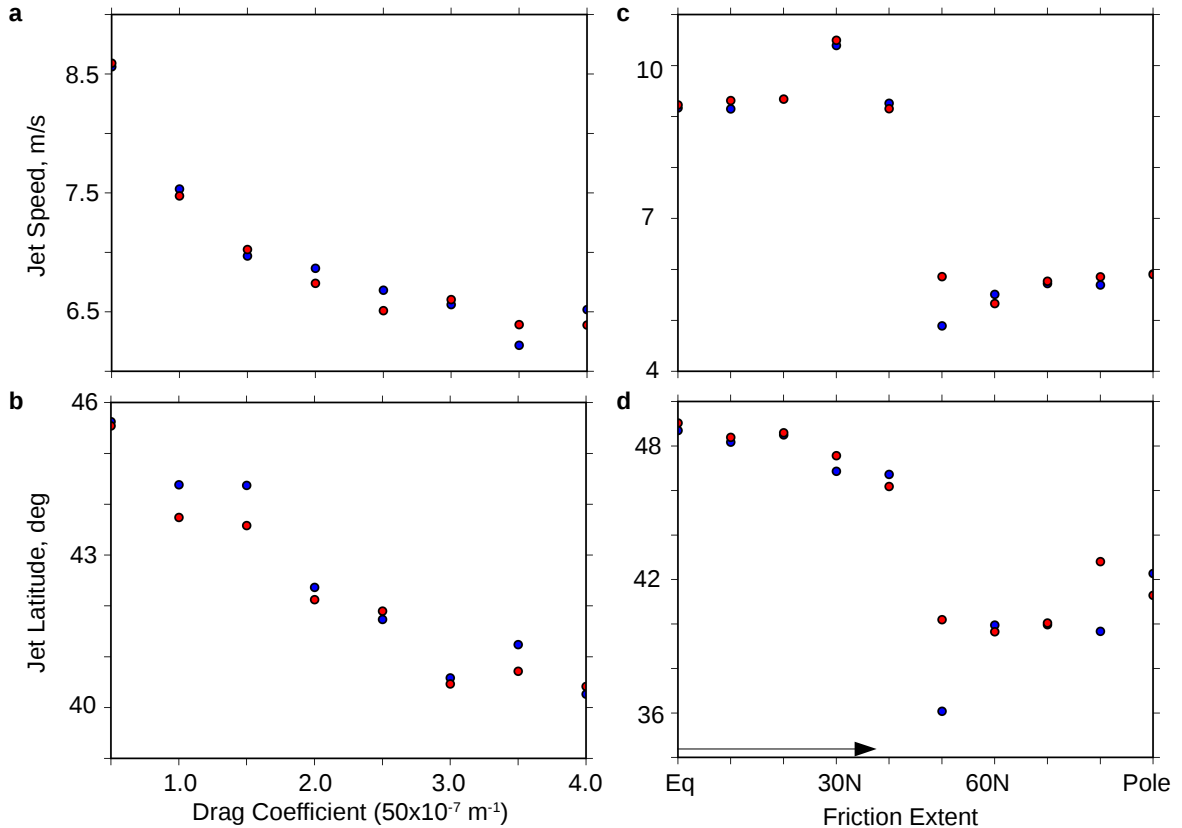
887 **Fig. 13.** Longitude profiles of the near-surface zonal wind speed along the jet axis for simulations in  
888 which the longitudinal extent of the near-surface drag within the baroclinic zone is enhanced  
889 relative to the rest of the globe. The dashed-vertical line denotes the drag extent for the  
890 jet-speed profile of same color. The black lines show the no-drag enhancement and the  
891 axisymmetric-drag enhancement cases. . . . .

56

892	<b>Fig. 14.</b> Filled, colored contours: the zonal wind anomaly field for simulations in which drag is enhanced in the baroclinic zone, relative to the unperturbed simulation (black, unfilled contours). The vertical magenta lines show the longitudinal extent of the enhanced drag in the baroclinic zone (the region between the dashed, green lines). In all simulations, the enhanced near-surface drag starts at 0°E. . . . .	57
897	<b>Fig. 15.</b> Similar to Fig. 14., but for the field of near-surface meridional transient-eddy temperature fluxes $\overline{v'T'} \cos \varphi$ . The overline represents a temporal mean, while the primes represent departures therefrom. . . . .	58
900	<b>Fig. 16.</b> Similar to Fig. 14., but for the field of near-surface meridional stationary eddy temperature fluxes $\bar{v}^* \bar{T}^* \cos \varphi$ in the color shading and the near-surface stationary temperature anomaly $\bar{T}^*$ in the black contours. The asterisks represent departures from a zonal mean. . . . .	59
904	<b>Fig. 17.</b> The sensitivity of a fluid parcel's latitude to an externally forced change in its zonal wind speed, under the assumption of angular momentum conservation. The numbers show the change in latitude assuming a 1 m/s change in the zonal-mean zonal wind speed. . . . .	60
906	<b>Fig. 18.</b> Zonal-mean profiles of the Bernoulli function (c) and its components (a and b), computed for the control simulation, which has no enhanced drag. The profiles are computed using near-surface, vertical averages between $\sigma = 0.84$ and $\sigma = 0.93$ . a: Mean kinetic energy, b: Geopotential, and c. The Bernoulli function. Each colored line represents a 90-day average over the control simulation, which is in a statistically steady state and has been spun up for 1800 days. The black vertical lines bound the baroclinic zone and mark the eddy-driven jet maximum. . . . .	61



913 FIG. 1. The eddy-driven jet speed (a) and latitude (b) response to global drag variations. The eddy-driven  
 914 jet is measured using zonal-mean zonal winds averaged between  $\sigma = 0.8$  and  $\sigma = 0.6$ . The blue dots show the  
 915 southern hemisphere, while the red dots show the statistically-independent northern hemisphere. The error bars  
 916 show the 95% confidence interval about the jet's mean speed and latitude.



917 FIG. 2. The eddy-driven jet speed (a, c) and latitude (b, d) response to boundary-layer drag. (a, b): jet  
 918 response to changes in boundary-layer drag within the baroclinic zone, the constant-width region between 35  
 919 N/S and 55 N/S. (c, d): jet response to near-surface drag that extends from the equator to the latitude specified  
 920 on the abscissa. The eddy-driven jet is defined using the zonal-mean zonal winds averaged between  $\sigma = 0.8$  and  
 921  $\sigma = 0.6$ . The blue dots show the Southern Hemisphere, while the red dots show the statistically-independent  
 922 Northern Hemisphere.

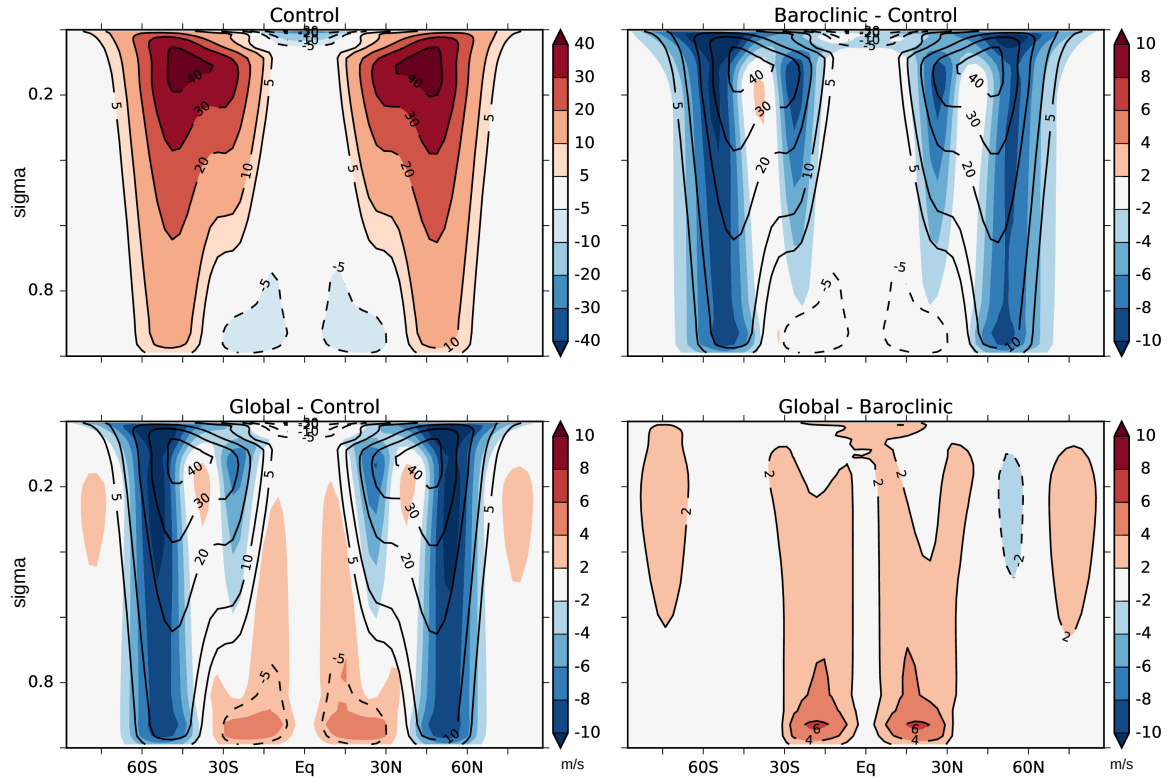


FIG. 3. The latitude-sigma zonal-mean zonal wind field for 1) a control simulation with unperturbed near-surface drag 2) the globally enhanced near-surface drag simulation minus the control simulation 3) the enhanced near-surface drag within the baroclinic zone simulation minus the control simulation and 4) the globally enhanced drag simulation minus drag enhanced within the baroclinic zone simulation. The baroclinic zone is the axisymmetric region between  $\pm 35^\circ\text{N}$  and  $\pm 55^\circ\text{N}$ . The black, unfilled contours, save for those in one panel, show the zonal-mean zonal wind field in the control simulation. The enhanced drag value used in the perturbed simulations is  $64 \times 10^{-7} \text{ m}^{-1}$ .

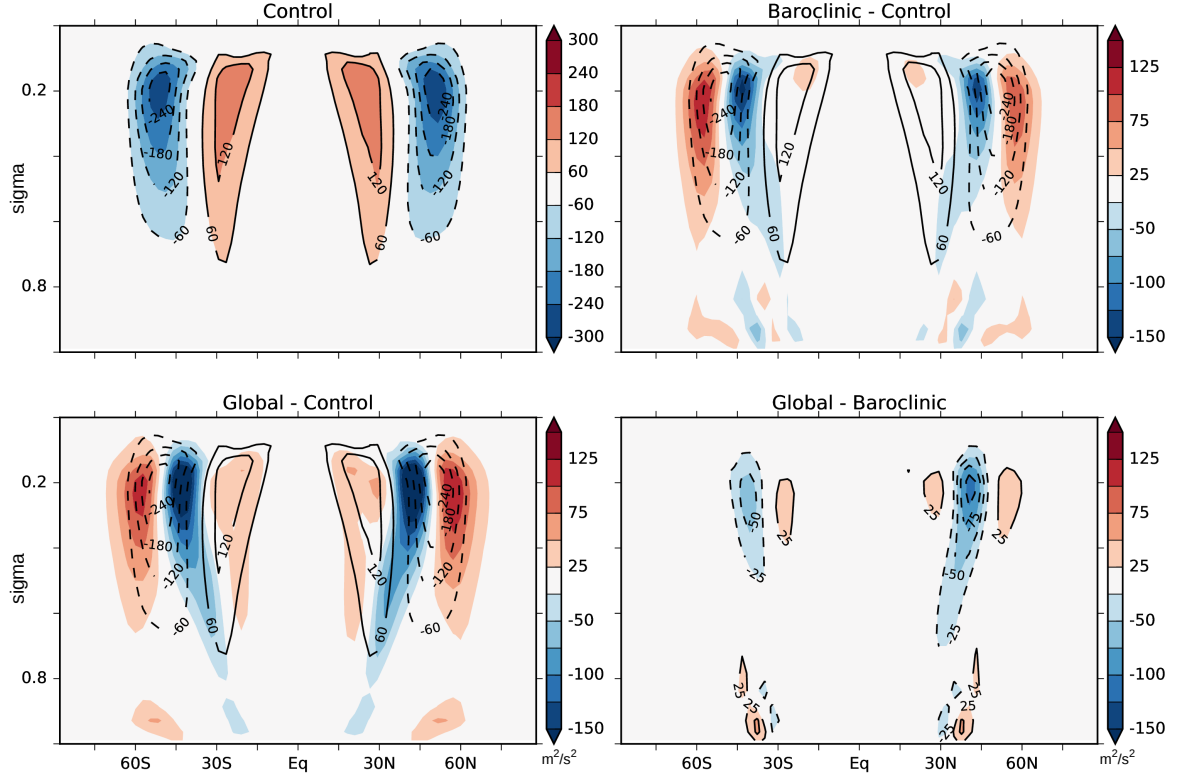
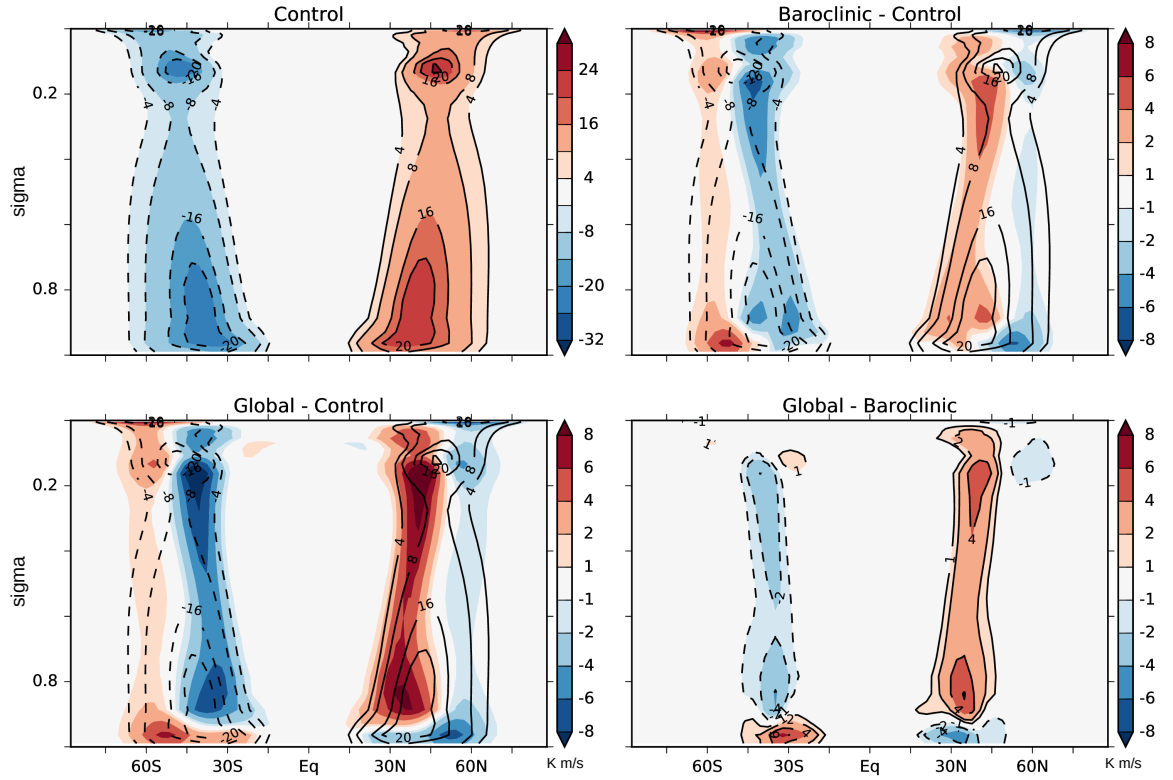
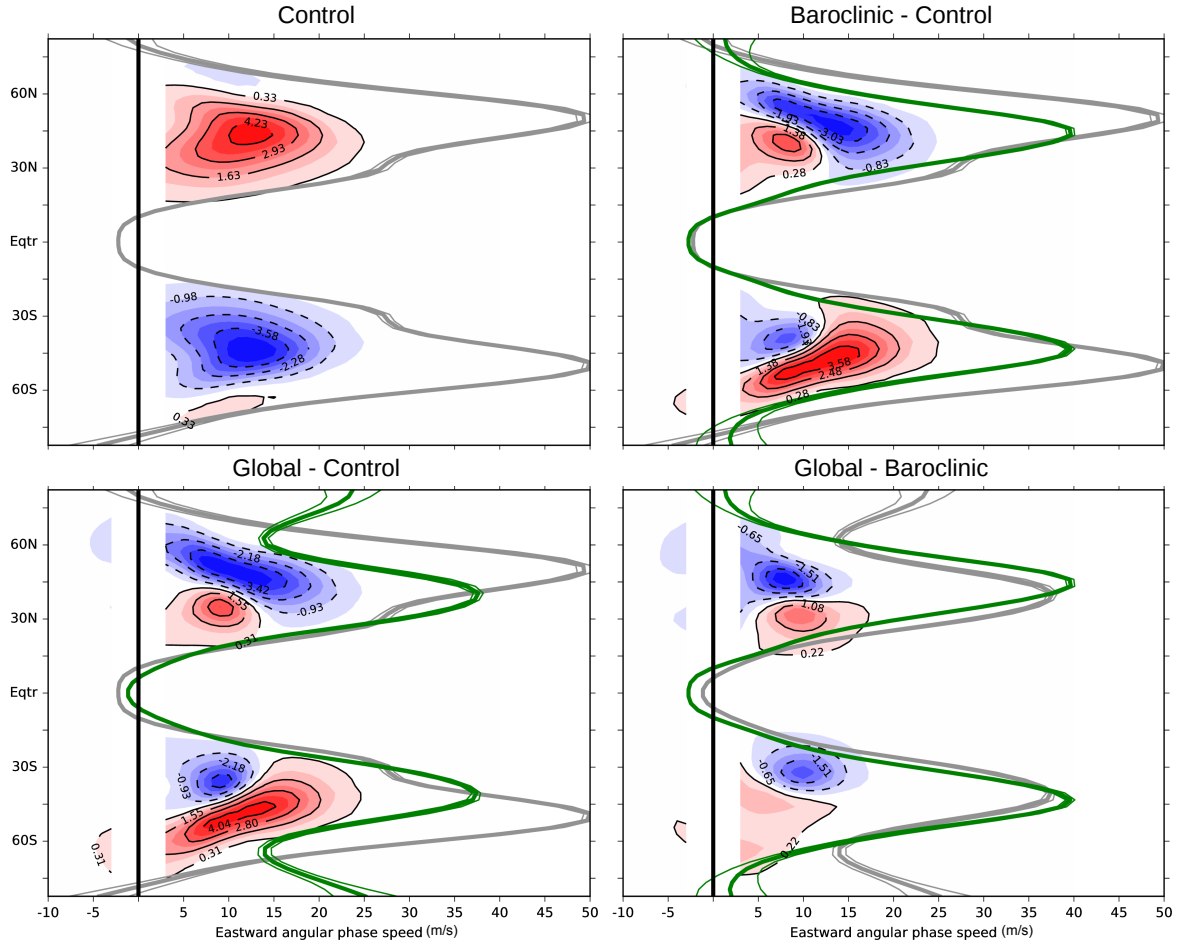


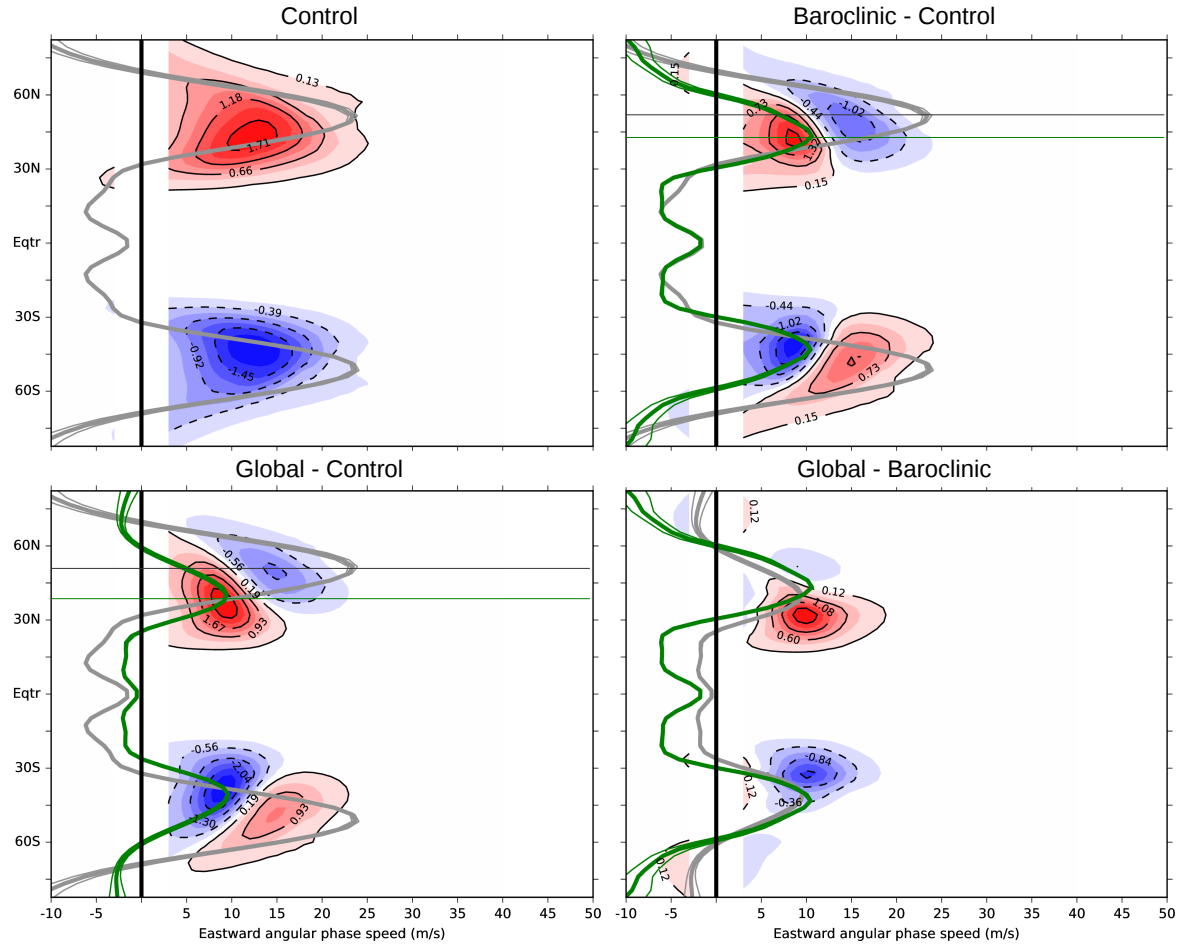
FIG. 4. The latitude-sigma eddy momentum flux divergence  $\partial_\phi (\bar{u}'v' \cos \phi) / (R \cos \phi)$  field for 1) a control simulation with no enhanced near-surface drag 2) the globally enhanced near-surface drag simulation minus the control simulation 3) the near-surface drag enhanced in the baroclinic zone simulation minus the control simulation and 4) the globally enhanced drag simulation minus the drag enhanced in the baroclinic zone simulation. The baroclinic zone is the axisymmetric region between  $\pm 35^\circ\text{N}$  and  $\pm 55^\circ\text{N}$ . The black, unfilled contours, save for those in one panel, show the field of eddy momentum flux divergence in the control simulation. We have multiplied by the constant radius of Earth to obtain units of  $m^2/s^2$ .



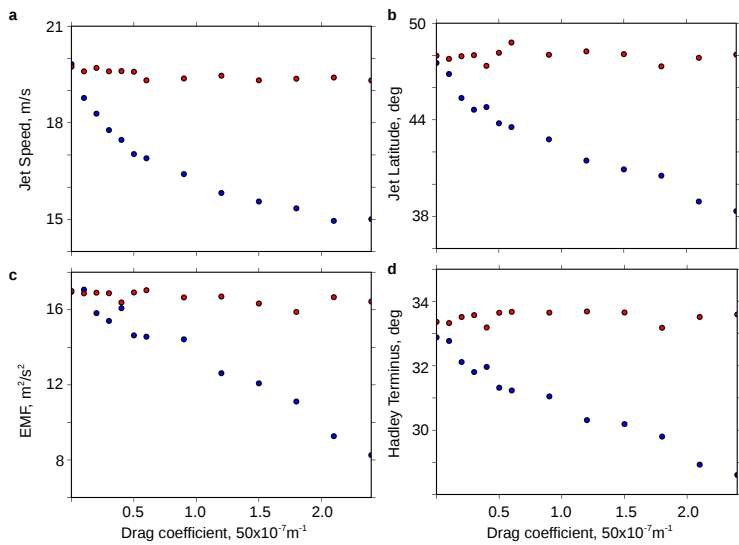
937 FIG. 5. The latitude-sigma meridional eddy heat fluxes  $\bar{v}'\theta'$  field for 1) a control simulation with no enhanced  
 938 near-surface drag 2) the globally enhanced near-surface drag simulation minus the control simulation 3) the  
 939 near-surface drag enhanced in the baroclinic zone simulation minus the control simulation and 4) the globally  
 940 enhanced drag simulation minus drag enhanced in the baroclinic zone simulation. The baroclinic zone is the  
 941 axisymmetric region between  $\pm 35^\circ\text{N}$  and  $\pm 55^\circ\text{N}$ . The black, unfilled contours, save for those in one panel,  
 942 show the field of eddy heat fluxes in the control simulation.



943 FIG. 6. The contours in the control simulation show the phase-speed spectrum of upper-level (300 hPa)  
 944 northward momentum fluxes. The thick gray line in the control simulation shows the meridional profile of the  
 945 upper-level westerly wind, which has been normalized by the cosine of latitude. The contours in the remaining  
 946 plots show differences in the northward momentum fluxes. The thick green lines show the normalized westerly  
 947 wind in the perturbed simulations. The thin lines bounding the westerlies are twice the standard error of a  
 948 30-member ensemble mean.



949 FIG. 7. The contours in the control simulation show the phase-speed spectrum of near-surface (850 hPa)  
950 northward temperature fluxes. The thick gray line in the control simulation shows the meridional profile of the  
951 near-surface westerly wind, which has been normalized by the cosine of latitude. The contours in the remaining  
952 plots show differences in the northward temperature fluxes. The thick green lines show the normalized westerly  
953 wind in the perturbed simulations. The thin lines bounding the westerlies are twice the standard error of a  
954 30-member ensemble mean. The thin horizontal lines mark the Northern Hemisphere westerly wind maximum.



955 FIG. 8. The jet-speed (a), jet-latitude (b), vertically-averaged eddy momentum fluxes (c), and the Hadley cell  
 956 terminus latitude (d) responses to variations in boundary-layer drag in the Southern Hemisphere. The blue dots  
 957 show values for the Southern Hemisphere, while the red dots show values for the Northern Hemisphere. The  
 958 error bars are computed using a boot-strap procedure.

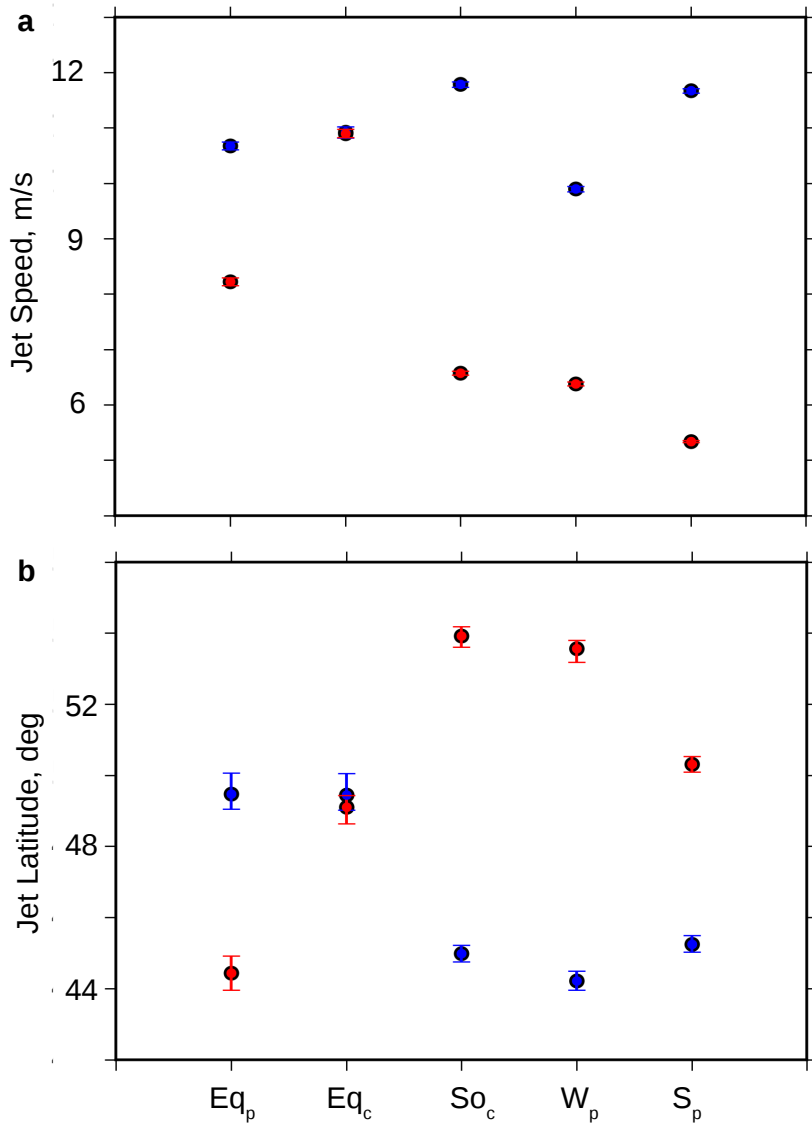
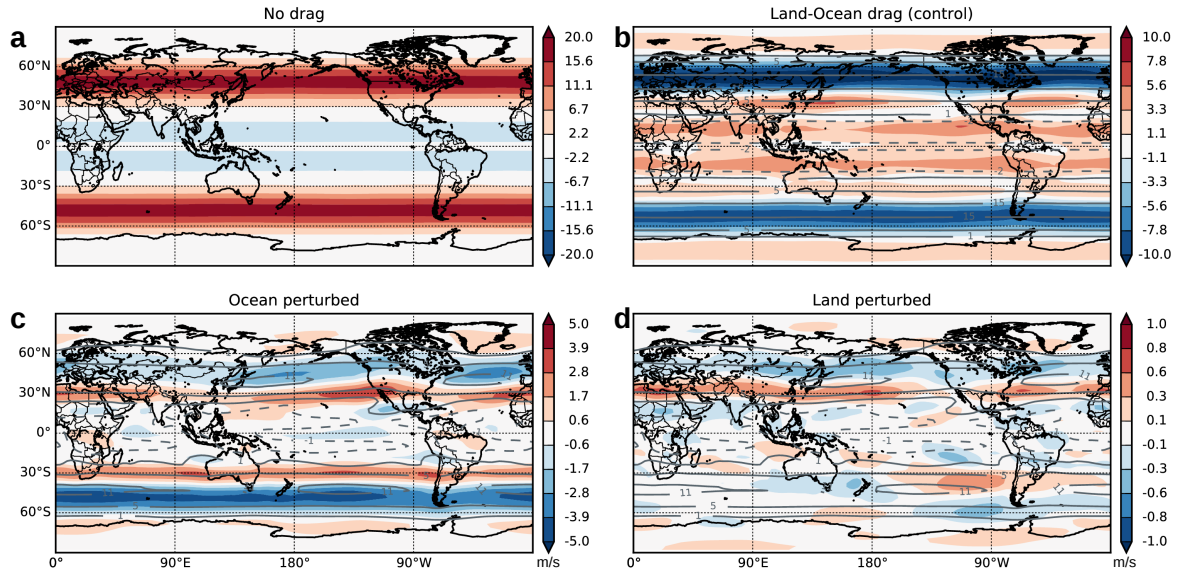
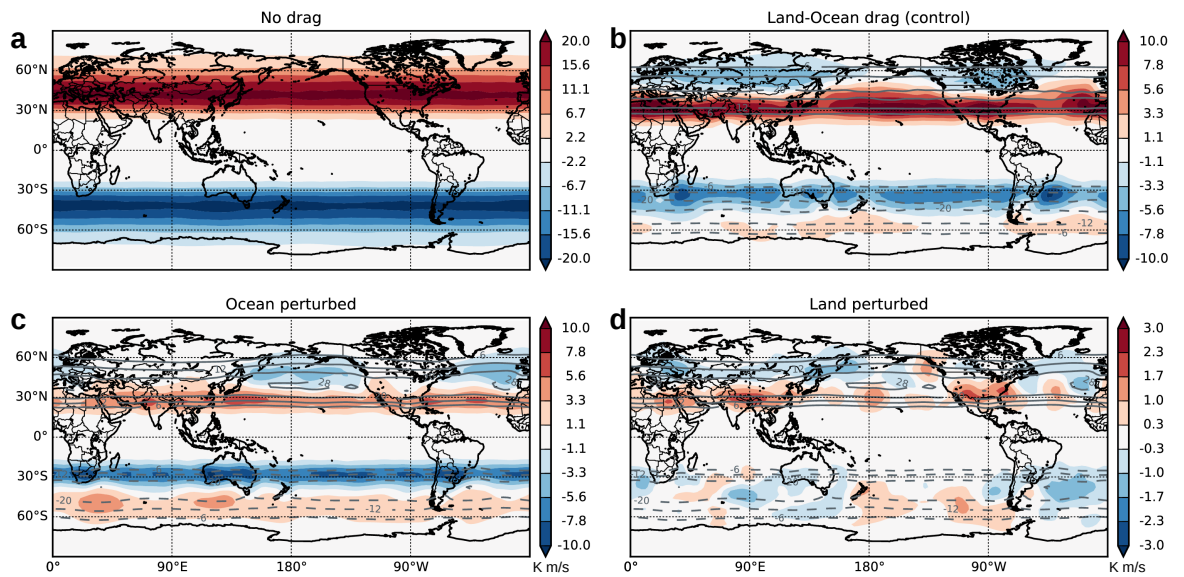


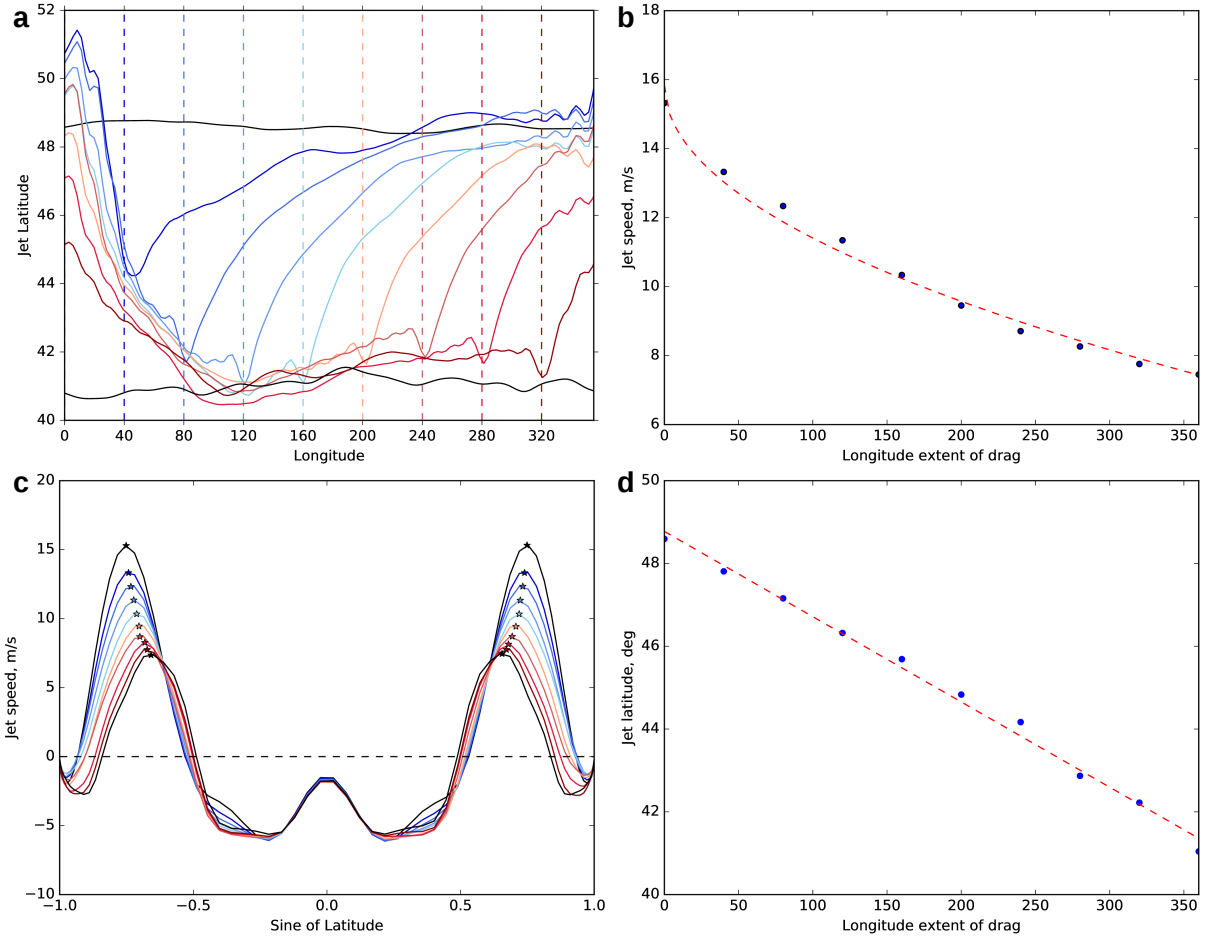
FIG. 9. Jet speed (a) and latitude (b) for three simulations in which boundary-layer friction is perturbed, one unperturbed equinox control simulation Eq<sub>c</sub>, and one unperturbed solstice control simulation So<sub>c</sub>. Eq<sub>p</sub> shows jet speed and latitude for increased near-surface friction in the hemisphere indicated in red in an equinox profile; W<sub>p</sub> shows the two metrics for increased near-surface friction in the winter hemisphere; while S<sub>p</sub> shows it for the summer hemisphere. In the solstice profile simulations, the blue dots show the winter hemisphere, while the red dots show the summer hemisphere. The error bars show a 95% confidence interval for the mean.



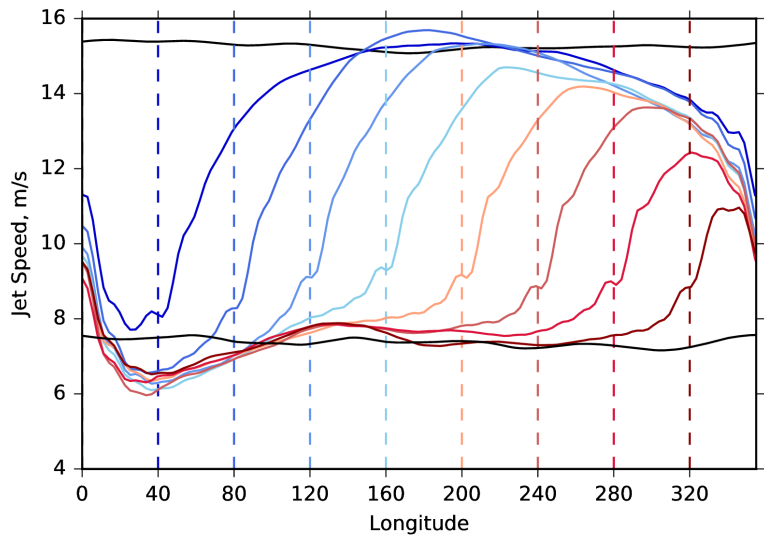
965 FIG. 10. Near-surface zonal wind response to variations in boundary-layer drag. a: Near-surface zonal  
 966 winds in the no enhanced drag simulation. b: The Earth-like boundary-layer drag simulation minus the no  
 967 enhanced drag simulation (filled, colored contours) and the near-surface zonal winds from the no enhanced  
 968 drag simulation (grey, unfilled contours). c: Enhanced drag over the oceans simulation minus the Earth-like  
 969 boundary-layer drag simulation (filled, colored contours) and the near-surface zonal winds from the Earth-like  
 970 boundary-layer drag simulation (gray, unfilled contours). d: Enhanced drag over the land simulation minus the  
 971 Earth-like boundary-layer drag simulation (filled, colored contours) and the near-surface zonal winds from the  
 972 Earth-like boundary-layer drag simulation (gray, unfilled contours).



973 FIG. 11. Similar to Fig. 10., but for the storm-track response to variations in boundary-layer drag. The storm  
 974 track is identified using near-surface meridional eddy heat fluxes  $\bar{v}'\theta'$ .



975 FIG. 12. a: Longitude profiles of the extremum of the near-surface zonal wind (the jet axis) for simulations  
 976 in which the longitudinal extent of the near-surface drag within the baroclinic zone is enhanced relative to the  
 977 rest of the globe. The dashed-vertical lines denote the drag extent for jet axis profiles of same color. The black  
 978 lines show the no enhancement and the axisymmetric enhancement cases. b: The zonal-mean jet speed response  
 979 to increases in the longitudinal extent of near-surface drag. The dashed, red curve shows a non-linear fit to the  
 980 GCM's output. c: The near-surface zonal-mean zonal wind profile response to changes in the longitudinal extent  
 981 of near-surface baroclinic zone drag. The star indicates the computed location of the jet. The color scheme is  
 982 that same as in Fig. 10a. d: The zonal-mean jet latitude response to increases in the longitudinal extent of  
 983 near-surface drag. The dashed, red line shows a linear fit to the GCM's output.



984 FIG. 13. Longitude profiles of the near-surface zonal wind speed along the jet axis for simulations in which  
985 the longitudinal extent of the near-surface drag within the baroclinic zone is enhanced relative to the rest of the  
986 globe. The dashed-vertical line denotes the drag extent for the jet-speed profile of same color. The black lines  
987 show the no-drag enhancement and the axisymmetric-drag enhancement cases.

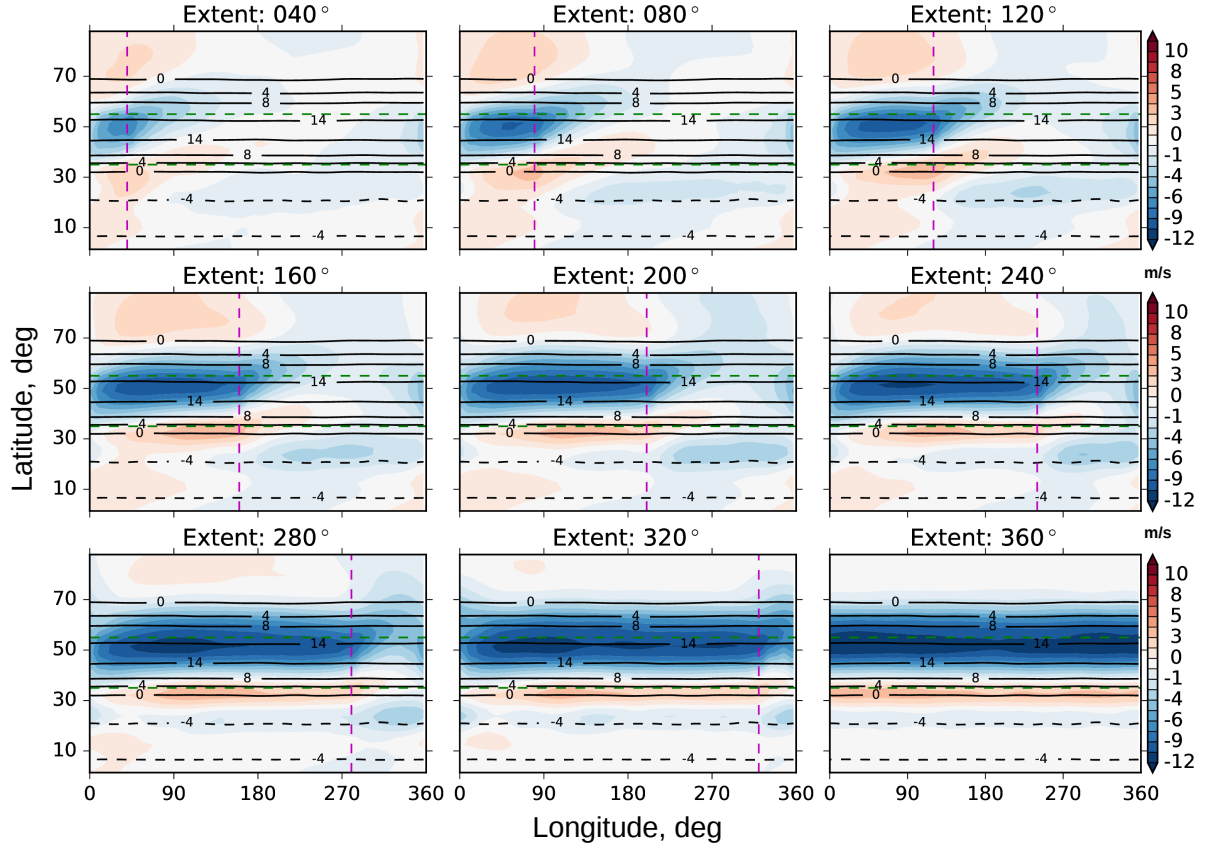
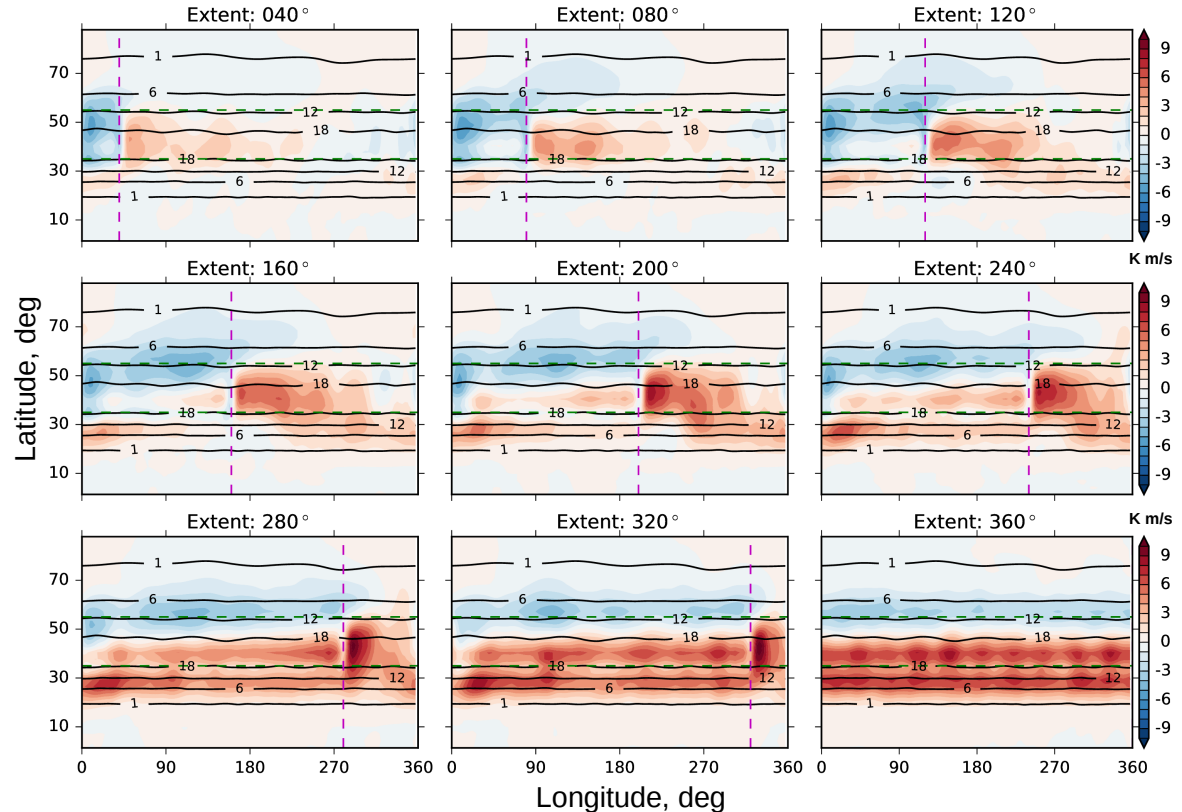
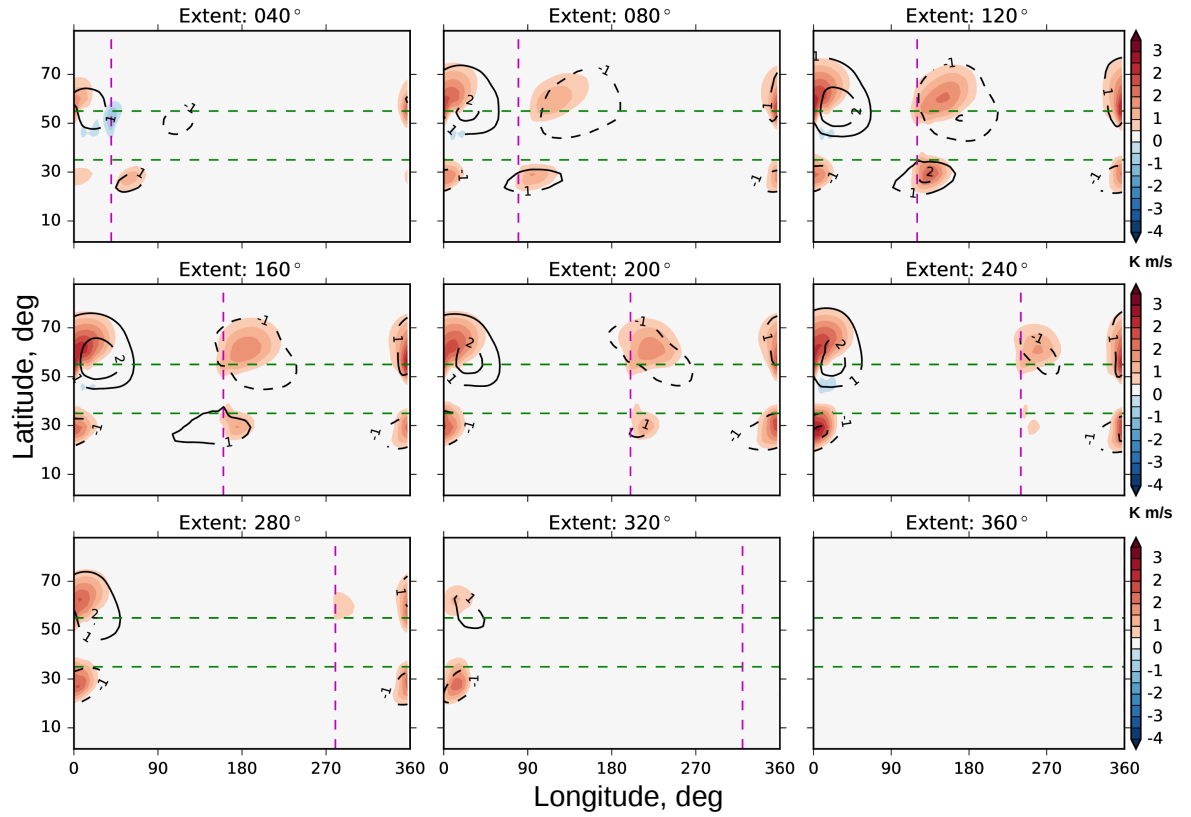


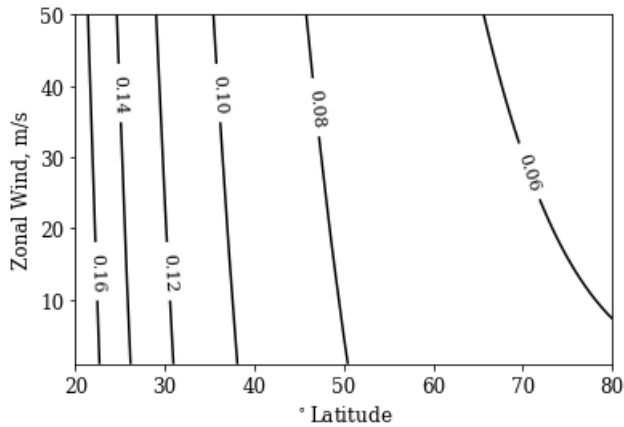
FIG. 14. Filled, colored contours: the zonal wind anomaly field for simulations in which drag is enhanced in the baroclinic zone, relative to the unperturbed simulation (black, unfilled contours). The vertical magenta lines show the longitudinal extent of the enhanced drag in the baroclinic zone (the region between the dashed, green lines). In all simulations, the enhanced near-surface drag starts at  $0^{\circ}\text{E}$ .



992 FIG. 15. Similar to Fig. 14., but for the field of near-surface meridional transient-eddy temperature fluxes  
993  $\overline{v' T'} \cos \varphi$ . The overline represents a temporal mean, while the primes represent departures therefrom.



994 FIG. 16. Similar to Fig. 14., but for the field of near-surface meridional stationary eddy temperature fluxes  
995  $\bar{v}^* \bar{T}^* \cos \varphi$  in the color shading and the near-surface stationary temperature anomaly  $\bar{T}^*$  in the black contours.  
996 The asterisks represent departures from a zonal mean.



997 FIG. 17. The sensitivity of a fluid parcel's latitude to an externally forced change in its zonal wind speed,  
 998 under the assumption of angular momentum conservation. The numbers show the change in latitude assuming a  
 999 1 m/s change in the zonal-mean zonal wind speed.

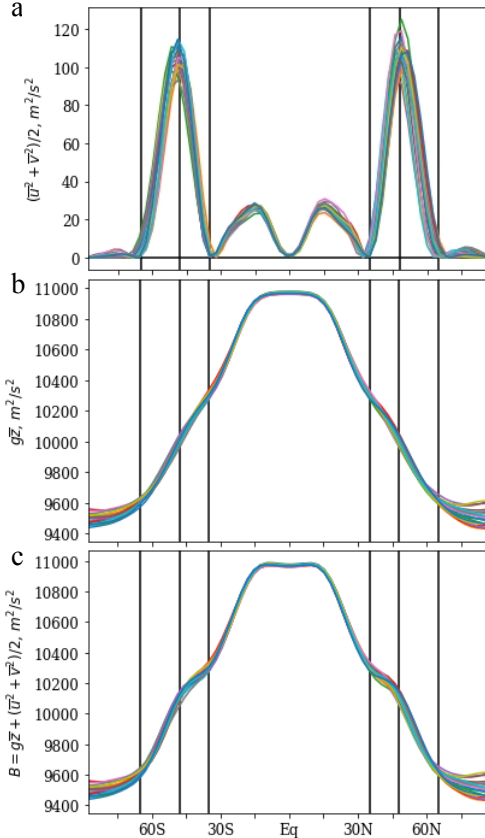


FIG. 18. Zonal-mean profiles of the Bernoulli function (c) and its components (a and b), computed for the control simulation, which has no enhanced drag. The profiles are computed using near-surface, vertical averages between  $\sigma = 0.84$  and  $\sigma = 0.93$ . a: Mean kinetic energy, b: Geopotential, and c. The Bernoulli function. Each colored line represents a 90-day average over the control simulation, which is in a statistically steady state and has been spun up for 1800 days. The black vertical lines bound the baroclinic zone and mark the eddy-driven jet maximum.